Title: Abrupt CO_2 release to the atmosphere under glacial and early interglacial climate conditions

Authors: C. Nehrbass-Ahles[1,2,3*], J. Shin[4], J. Schmitt[1,2], B. Bereiter[1,2,5], F. Joos[1,2], A. Schilt[1,2], L. Schmidely[1,2], L. Silva[1,2], G. Teste[4], R. Grilli[4], J. Chappellaz[4], D. Hodell[3], H. Fischer[1,2], and T. F. Stocker[1,2].

Affiliations:

[1]Climate and Environmental Physics, Physics Institute, University of Bern, Switzerland

[2]Oeschger Centre for Climate Change Research, University of Bern, Switzerland

[3]Godwin Laboratory for Palaeoclimate Research, Department of Earth Sciences, University of Cambridge, UK

[4]IGE, Grenoble INP, IRD, CNRS, Univ. Grenoble Alpes, France

[5]Laboratory for Air Pollution / Environmental Technology, Empa, Dübendorf, Switzerland

*Correspondence to: cn425@cam.ac.uk

Abstract: Pulse-like CO_2 release to the atmosphere on centennial timescales has only been identified for the most recent glacial and deglacial periods and is thought to be absent during warmer climate conditions. Here, we present a high-resolution CO_2 record from 330,000 to 450,000 years before present, revealing pronounced Carbon Dioxide Jumps (CDJ) under cold and warm climate conditions. CDJ come in two varieties that we attribute to invigoration or weakening of the Atlantic Meridional Overturning Circulation and associated northward and southward shifts of the Intertropical Convergence Zone, respectively. We find that CDJ are pervasive features of the carbon cycle that can occur during interglacial climate conditions if land ice masses are sufficiently extended to be able to disturb the Atlantic Meridional Overturning Circulation by freshwater input.

One Sentence Summary: Ice core record reveals centennial-scale CO_2 releases to the atmosphere under past cold and warm climate states.

Main Text: Analyses of Antarctic ice cores have demonstrated that atmospheric CO_2 has been a major driver of Earth's climate on orbital to millennial time scales (*1-3*). However, evidence of sub-millennial scale CO_2 variability is only available for the last ~60 thousand years (ka), i.e., not beyond the last glacial period (e.g., *4-6*). Climate-carbon cycle perturbations during previous interglacial periods serve as first-order templates for the natural response of Earth's climate system to warmer climatic background conditions (*7*), but so far the use of CO_2 records to decipher sub-millennial scale variations has been hampered by insufficient temporal resolution of existing ice core records.

Previous research identified two principal modes of CO_2 variability on millennial to centennial time scales: (i) millennial-scale Carbon Dioxide Maxima (CDM) frequently occurring during the last glacial period (*4, 5, 8*) and (ii) centennial-scale Carbon Dioxide Jumps (CDJ) caused by pulse-like CO_2 releases to the atmosphere, most prominently occurring during the last deglaciation (*6, 9*).

CDM are characterized by a triangular shape of evolving CO_2 changes. They closely covary with Antarctic temperature proxy records on millennial timescales as evidenced by the Antarctic Isotope Maxima (*4, 8, 10*). During cold periods (stadials) in the Northern Hemisphere (NH), CO_2 is observed to increase gradually and in parallel to the bipolar seesaw response in Antarctic temperature (*11*) at typical rates of ~1 ppm per century (*4, 8*). CDM reach amplitudes of up to 30 ppm before their trends are reversed connected with a sudden strengthening of the Atlantic Meridional Overturning Circulation (AMOC) linking the onset of Dansgaard-Oeschger (DO) events (i.e., abrupt warming over Greenland) and the start of slow cooling in the Southern Ocean (SO) region (*4, 8, 11*).

In contrast, abrupt CDJ do not directly correspond to variations in Antarctic temperature but are associated with either DO events or Heinrich Stadials (HS) in the NH (*6, 12, 13*). The latter are characterized by extended cold periods in the NH associated with a

weakened AMOC (*14-16*). The few CDJ identified so far are superimposed on gradually increasing millennial CO_2 trends connected to CDM or glacial terminations and lead to a sudden 10 to 15 ppm CO_2 rise within less than ~250 years at rates of ~10 ppm per century, about ten times faster than CDM. As of yet, CDJ have only been identified during the last deglaciation (Termination I) (*6, 9*) and for HS 4 (*12, 13*), occurring at 39.5 ka BP (thousand years before present, defined as 1950 CE). CDJ are synchronous with either major methane (CH_4) rises linked to DO events or small CH_4 peaks associated with HS, suggesting a link with sudden AMOC changes and poleward shifts of the Intertropical Convergence Zone (ITCZ) (*6, 17, 18*). Here we address whether CDJ also occur during glacial growth phases and interglacial climate conditions and therefore whether they are a pervasive feature of the past carbon cycle.

Centennial to millennial-scale CO_2 variability between ~150 and 400 ka BP could not be explored because of insufficient measurement precision and low temporal resolution of the existing CO_2 record available for this period (*1*). Here we investigate the older part of this interval by presenting a high-resolution record of CO_2 mole fractions covering a full glacial-interglacial cycle from 330 to 450 ka BP [i.e., Marine Isotope Stage (MIS) 9e - 12a (*19*)], measured on samples from the EPICA Dome C (EDC) ice core using an improved dry-extraction technique (*20*). In comparison to earlier data (*1, 2*), we enhance the precision by a factor of three (now ~1 ppm) and increase temporal resolution four to six times (now ~300 years on average).

Together with CO_2 we improve the resolution of the existing EDC CH_4 record (*21*) to an average of ~250 years at periods of abrupt changes (*20*). This permits a direct comparison of the CH_4 imprint of fast climate changes in the NH with the Southern Hemisphere bipolar seesaw response in Antarctic temperature and atmospheric CO_2 (*4, 8*). We combine our ice core data with new records of benthic $\delta^{13}C$ and $\delta^{18}O$ of *C. wuellerstorfi* (*22*) and planktic

$\delta^{18}O$ of *G. bulloides* (*23*). These stable isotope data are measured on marine sediment core samples from the International Ocean Discovery Program (IODP) Site U1385 located on the Iberian Margin off the coast of Portugal in a water depth of ~2600 m below sea level (*20*). A temporal resolution of ~150 years on average enables us to directly compare our ice core data to this independent paleoclimatic archive of hydrological change in the North Atlantic (NA).

On orbital timescales, the new CO_2 record reveals generally high CO_2 levels persisting above 260 ppm (*24*) over ~35 ka during the exceptionally long interglacial period MIS 11c - e from 427 to 393 ka BP (Fig. 1B) extending over more than one precessional cycle (*25*). The minimum CO_2 value of 187.6±1.0 ppm is reached at 358 ka BP coinciding with the lowest sea surface temperature (SST) [Fig. 2D, 2G, and 2H, (*26*)]. However, the onset of the deglacial CO_2 rise towards MIS 9e (Termination IV), only takes place ~13.5 ka later at 344.5 ka BP. The end of this deglacial CO_2 increase (~335 ka BP) is marked by a peak CO_2 value of 300.4±1.0 ppm, representing the highest natural CO_2 mole fraction derived from Antarctic ice cores over the past 800 ka. Superimposed on this orbital trend we identify different types of millennial to centennial-scale CO_2 variability, occurring most frequently during, but not limited to, the glacial growth phase.

On millennial timescales, the CO_2 record mirrors the variability in the EDC temperature proxy [Fig. 1A, 2A, (*10*)] and dust flux records [Fig. 2B, (*27*)], a feature previously observed over the last 800 ka in lower resolution CO_2 data (*2, 3*). Our new benthic $\delta^{18}O$ record from the IODP Site U1385 follows the same pattern (Fig. 2C) indicating the influence of southern-sourced deep-water as first noted for the last glacial period (MIS 3) (*28*). Our results demonstrate that this correlation also applies to MIS 10a - 11a, thereby emphasizing the key role of SO processes in the bipolar seesaw (*4, 11*) and associated global-scale climate regime shifts in shaping atmospheric CO_2 on millennial timescales. We identify in total seven CDM events (Fig. 1B). The two youngest events (CDM 9e and 10b) were

identified previously (*1*), but not the oldest five (CDM 11a.1 to 11e). Furthermore, our record shows that the covariation of CO_2 and the Antarctic temperature proxy (*10*) holds also for the extended interglacial period MIS 11c (Fig. 1A, 1B), where both Antarctic temperatures and CO_2 gradually increase along with the summer insolation at 65°N (*25*). The time where CO_2 and Antarctic temperature cease to covary in our record is at the end of MIS 11c, when Antarctic temperature leads the CO_2 decrease by several thousand years, similar to what is observed for the glacial inception after the penultimate interglacial (*29*).

On the centennial timescale, we detect eight CDJ occurring under very different climate boundary conditions (Fig. 1B). They are marked by centennial-scale peaks in the rate of change of CO_2 exceeding a threshold of 1.5 ppm per century in the ice core record [Fig. 1D, (*20*)]. The close correlation of millennial-scale CO_2 variability with Antarctic temperature (Fig. 1A) does not hold for CDJ (Fig. 3A, S1A). While all CDJ lead to an abrupt ~10 ppm rise in CO_2 (Table S1), their underlying causes may be different (*13, 30*). We distinguish two varieties of CDJ based on the presence (or absence) of a major simultaneous CH_4 rise at the same depth level of the ice core (*20*).

The first variety of CDJ is synchronous with rapid rises in the CH_4 record greater than 50 ppb (Fig. 1C, 3C) and growth rates exceeding 20 ppb per century as recorded in the EDC ice core (Fig. 1E, 3E). We dub these pulse-like CO_2 release events CDJ+. Following this definition, we identify five new CDJ+ (9e, 11a.2 - 4, and 11e; Fig. 1B). The major CH_4 rises associated with CDJ+ indicate abrupt DO-like warming in the NH directly linked to AMOC invigorations (*6, 17*). Direct evidence for such AMOC strengthening comes from associated abrupt rises in SST in the NH (Fig. 2F - H) and increases of benthic $\delta^{13}C$ values (Fig. 2I), indicative of the inflow of NA deep-water masses at IODP Site U1385. These findings are consistent with the two previously identified CDJ+ events during the last deglaciation at the onsets of the Bølling-Allerød and Preboral periods (*6, 9*).

The most pronounced CDJ+ (CDJ+ 9e) takes place during early interglacial conditions when CO_2 values are already above 285 ppm, a level that is higher than typical peak CO_2 mole fractions during interglacial conditions over the past 800 ka (*3*). The time resolution for CDJ+ 9e is better than 90 years and shows an exceptionally fast CO_2 increase of ~10 ppm per century, as preserved in the ice archive. Accounting for the smoothing of atmospheric signals by the bubble enclosure process, we estimate an original rate of atmospheric CO_2 increase of 26.2±17.6 ppm per century [Fig. 3B, Table S1, (*20*)]. This provides a benchmark of the possible range and speed of positive carbon cycle feedbacks connected to AMOC variations during the deglaciation. This rate exceeds previous estimates of maximum pre-industrial atmospheric increase rates (*31*) by a factor of seven, but this is still a factor of nine lower than recent anthropogenic growth rates over the past decade (*32*). The CO_2 decrease after CDJ+ 9e shows that natural processes during interglacial conditions allowed for a sustained CO_2 removal from the atmosphere estimated at ~2 ppm per century for about 2 ka (Fig. 1B, 3B).

The second variety of CDJ occurs independently from major responses in the EDC CH_4 record (Fig. 1E, 3C, 3E, see supplementary text) and is dubbed CDJ−. We identify two CDJ− (10a and 11a.2), which share similar characteristics with the two CDJ− events associated with HS 1 during the last deglaciation (~16 ka BP) and HS 4 (*6, 12, 13*). We speculate that CDJ− can be attributed to carbon cycle processes caused by AMOC weakening. Although direct AMOC records do not yet exist for MIS 9e - 12a, abrupt decreases of benthic $\delta^{13}C$ indicate intrusions of Antarctic Bottom Water masses at IODP Site U1385 (Fig. 2I) likely due to AMOC weakening, similar to that which happened during HS in the last glacial period (*14, 15*). Note that major HS (HS 10.1 and HS 10.2) are identified in Fig. 2 by the drop in $U^{k'}_{37}$-based sea surface temperature (Fig. 2G) and the decrease in benthic $\delta^{13}C$ (Fig. 2I) indicative of a reduced state of the AMOC. While CDJ− 10a is likely

related to carbon cycle responses to an AMOC slow-down caused by massive ice discharge during HS 10.1 (Fig. 2I), there exists only ambiguous evidence for CDJ− 11a.2 being associated with freshwater forcing. Low CH_4 levels (Fig. 2E) and cold SST in the NA (Fig. 2F) indicate stadial conditions in the NH associated with CDJ− 11a.2. Given the relative age uncertainties between our ice core and independently dated records (*33, 34*), the $\delta^{18}O$ calcite record from Sanbao Cave [Fig. 2J, (*35*)] indicates a major shift of the ITCZ that may be associated with CDJ− 11a.2 (*18, 36*).

Most notably, the new CO_2 record reveals the clearly distinguishable CDJ 11c (12.9±2.7 ppm increase within 191±123 years, Fig. 3B, Table S1) at 415 ka BP, occurring ~10 ka into interglacial temperature conditions at Dome C, but still at a time of considerable sea level rise [Fig. 2K, (*37*)]. A hiatus in the section older than 407 ka BP at IODP Site U1385 obscures potential signals related to this event (*20*). A distinct peak found in a proxy for SST conditions at 412 ka BP [Fig. 2F, (*38*)] is indicative of hydrographic disturbance in the NA. A possible perturbation of the AMOC at the same time (*39*) may be connected to this event, both of which may be attributed to a major freshwater forcing at the time of near deglaciation of the southern Greenland Ice Sheet in the early part of MIS 11c (*40*). Another recent study suggests a major ice-sheet discharge event into the SO that might also coincide with this CDJ at 415 ka BP (*41*), but dating uncertainties do not permit an unambiguous attribution. While there is limited evidence supporting an AMOC perturbation around 415 ka BP, it remains unclear whether CDJ 11c is associated with an AMOC weakening or strengthening. Given the lack of a major CH_4 rise in our record (Fig. 3C, 3E) we classify this event as a CDJ− (CDJ− 11c); however, it could mechanistically also be a CDJ+, with an atypical CH_4 response caused by already warm climate conditions in the NH.

Invigorations of the AMOC during DO events lead to abrupt increases in cross-equatorial heat transport to the NH (*15, 42*), which may be a necessary (yet not a sufficient)

condition for the occurrence of CDJ+ events (*6, 43*). As a direct consequence of this energy imbalance the ITCZ shifts northward and promotes a poleward shift and intensification of westerlies in the NH (*18, 42*). Driven by this shift in the ITCZ, new tropical wetlands are formed in the NH, which leads to an extended increase in CH_4 production (*17, 18*).

Conversely, we presume that CDJ− are associated with a weakening of the AMOC causing a southward shift of the ITCZ which is promoting the formation of wetlands in the SH. The latter results in an initial overshoot in the CH_4 production that coincides with CDJ− during HS 1 and HS 4 (*18*). These small, short-lived CH_4 peaks of amplitudes smaller than ~50 ppb are distinct from major CH_4 rises associated with CDJ+; however, both CH_4 responses proceed at comparable growth rates. The absence of any short-lived CH_4 peaks related to CDJ– in our record (Fig. 3C, S1C) – similar to those found for HS 1 and HS 4 (*18*) – can be explained by a combination of relatively low sample resolution and the bubble enclosure process that smooths the EDC gas record. The latter results in the obliteration of any potential CH_4 peaks smaller than ~50 ppb lasting for less than 200 years (see supplementary text). Accordingly, we use the absence of a major CH_4 rise as a criterion to distinguish a CDJ– from a CDJ+. Whereas the climate conditions for CDJ+ are characteristic for DO events in the NH, CDJ− appear to be connected with major freshwater forcing and stadial conditions in the NH (*6, 13, 18*).

The strong correspondence of the CO_2 record with Antarctic temperature and benthic $\delta^{18}O$ at the Iberian Margin on the millennial time scale (Fig. 2A, 2C, 2D) suggests a causal link of CDM formation with SO processes (*8*). Proposed CDM generating mechanisms include perturbations in the carbon cycle owing to changes in deep SO ventilation related to changes in stratification, buoyancy forcing, and Southern Hemisphere westerlies (e.g., *44, 45*), variations of the southern sea ice edge (e.g., *46*), efficiency of the biological pump

caused by changes in either the magnitude of dust-induced iron fertilization (e.g., *44*), or mode changes in the AMOC (e.g., *47*).

On the contrary, the underlying CO_2 release mechanisms for the CDJ are poorly understood. Suggested marine mechanisms include outgassing due to increasing SST (*30*), rapid ventilation of accumulated respired carbon from intermediate-depth Atlantic (*43, 48*), or SO deep-water masses (*49, 50*). Despite the coherence of CDJ with AMOC changes, and associated deep-water reorganizations in the NA [Fig. 2I, (*6, 43*)], the carbon source for CDJ may not necessarily originate from the ocean. Proposed terrestrial sources include permafrost thawing in the NH (*51*), drought-induced biomass decomposition (*6, 30*), and changes in precipitation and vegetation distribution connected to ITCZ shifts (*18, 36*). To explain a 10 ppm CDJ in the atmosphere caused by carbon release from the land biosphere, ~80 Pg of carbon are needed (*52*). For most of these processes, a shift of the position of the ITCZ and resulting changes in the mid to high-latitude westerly winds (*53*) are necessary to couple the cross-equatorial heat transport in the NA to the global carbon cycle (*11, 42*).

In summary, our CO_2 record from the EDC ice core provides evidence for centennial-scale CDJ during glacial, deglacial and early interglacial conditions. These suggest fast, pulse-like CO_2 releases to the atmosphere during MIS 9e - 12a that are likely related to abrupt changes in AMOC (Fig. 2I) and shifts in the position of the ITCZ (Fig. 2E). Our data imply that CDJ are a pervasive feature of the natural carbon cycle that may go undetected in CO_2 records of insufficient temporal resolution and precision. We stress that such CDJ also occur during interglacial temperature conditions, as long as fresh-water discharge from remnant ice sheets persists and is able to disturb ocean circulation. Anthropogenic warming and the committed ice sheet melting and associated sea level rise over the coming millennia (*54*) constitute new drivers that might trigger ocean circulation changes, and hence, pulse-like CO_2

releases such as those detected in our record during an earlier interglacial period when AMOC was perturbed.

References and Notes:

1. J. R. Petit *et al.*, Climate and atmospheric history of the past 420,000 years from the Vostok ice core, Antarctica. *Nature* **399**, 429-436 (1999).
2. U. Siegenthaler *et al.*, Stable carbon cycle-climate relationship during the late Pleistocene. *Science* **310**, 1313-1317 (2005).
3. D. Lüthi *et al.*, High-resolution carbon dioxide concentration record 650,000-800,000 years before present. *Nature* **453**, 379-382 (2008).
4. B. Bereiter *et al.*, Mode change of millennial CO_2 variability during the last glacial cycle associated with a bipolar marine carbon seesaw. *Proc. Natl. Acad. Sci. U.S.A.* **109**, 9755-9760 (2012).
5. J. Ahn, E. J. Brook, Siple Dome ice reveals two modes of millennial CO_2 change during the last ice age. *Nat. Commun.* **5**, 3723 (2014).
6. S. A. Marcott *et al.*, Centennial-scale changes in the global carbon cycle during the last deglaciation. *Nature* **514**, 616-619 (2014).
7. H. Fischer *et al.*, Palaeoclimate constraints on the impact of 2°C anthropogenic warming and beyond. *Nat. Geosci.* **11**, 474-485 (2018).
8. J. Ahn, E. J. Brook, Atmospheric CO_2 and climate on millennial time scales during the last glacial period. *Science* **322**, 83-85 (2008).
9. E. Monnin *et al.*, Atmospheric CO_2 concentrations over the last glacial termination. *Science* **291**, 112-114 (2001).
10. J. Jouzel *et al.*, Orbital and millennial Antarctic climate variability over the past 800,000 years. *Science* **317**, 793-796 (2007).

11. T. F. Stocker, S. J. Johnsen, A minimum thermodynamic model for the bipolar seesaw. *Paleoceanography* **18**, 1087 (2003).

12. J. Ahn, E. J. Brook, A. Schmittner, K. Kreutz, Abrupt change in atmospheric CO_2 during the last ice age. *Geophysical Research Letters* **39**, 5 (2012).

13. T. K. Bauska *et al.*, Controls on millennial-scale atmospheric CO_2 variability during the last glacial period. *Geophys. Res.* **45**, 7731-7740 (2018).

14. S. R. Hemming, Heinrich events: Massive late Pleistocene detritus layers of the North Atlantic and their global climate imprint. *Rev. Geophys.* **42**, RG1005 (2004).

15. L. G. Henry *et al.*, North Atlantic ocean circulation and abrupt climate change during the last glaciation. *Science* **353**, 470-474 (2016).

16. Heinrich Stadials are directly linked to massive glacial ice and meltwater discharges from Hudson Strait known as Heinrich events.

17. M. Baumgartner *et al.*, NGRIP CH4 concentration from 120 to 10 kyr before present and its relation to a $\delta^{15}N$ temperature reconstruction from the same ice core. *Clim. Past* **10**, 903-920 (2014).

18. R. H. Rhodes *et al.*, Enhanced tropical methane production in response to iceberg discharge in the North Atlantic. *Science* **348**, 1016-1019 (2015).

19. L. B. Railsback, P. L. Gibbard, M. J. Head, N. R. G. Voarintsoa, S. Toucanne, An optimized scheme of lettered marine isotope substages for the last 1.0 million years, and the climatostratigraphic nature of isotope stages and substages. *Quat. Sci. Rev.* **111**, 94-106 (2015).

20. Materials and methods are available as supplementary materials at the Science website.

21. L. Loulergue *et al.*, Orbital and millennial-scale features of atmospheric CH_4 over the past 800,000 years. *Nature* **453**, 383-386 (2008).

22. Benthic $\delta^{13}C$ of *C. wuellerstorfi* reflects changes in deep-water ventilation related to reorganization of deep-ocean circulation and remineralization of organic carbon. The $\delta^{18}O$ signal of the same species indicates variations in deep-water temperatures.

23. Millennial-scale changes in the planktic $\delta^{18}O$ record of *G. bulloides* follow changes in the sea surface temperature in the North Atlantic.

24. P. C. Tzedakis *et al.*, Interglacial diversity. *Nat. Geosci.* **2**, 751-755 (2009).

25. P. C. Tzedakis *et al.*, Can we predict the duration of an interglacial? *Clim. Past* **8**, 1473-1485 (2012).

26. T. Rodrigues *et al.*, A 1-Ma record of sea surface temperature and extreme cooling events in the North Atlantic: A perspective from the Iberian Margin. *Quat. Sci. Rev.* **172**, 118-130 (2017).

27. F. Lambert, M. Bigler, J. P. Steffensen, M. Hutterli, H. Fischer, Centennial mineral dust variability in high-resolution ice core data from Dome C, Antarctica. *Clim. Past* **8**, 609-623 (2012).

28. N. J. Shackleton, M. A. Hall, E. Vincent, Phase relationships between millennial-scale events 64,000–24,000 years ago. *Paleoceanography* **15**, 565-569 (2000).

29. R. Schneider, J. Schmitt, P. Köhler, F. Joos, H. Fischer, A reconstruction of atmospheric carbon dioxide and its stable carbon isotopic composition from the penultimate glacial maximum to the last glacial inception. *Clim. Past* **9**, 2507-2523 (2013).

30. T. K. Bauska *et al.*, Carbon isotopes characterize rapid changes in atmospheric carbon dioxide during the last deglaciation. *Proc. Natl. Acad. Sci. U. S. A.* **113**, 3465-3470 (2016).

31. F. Joos, R. Spahni, Rates of change in natural and anthropogenic radiative forcing over the past 20,000 years. *Proc. Natl. Acad. Sci. U. S. A.* **105**, 1425-1430 (2008).

32. P. Tans, R. Keeling, "Annual mean CO_2 growth rate for Mauna Loa, Hawaii" (NOAA/ESRL and Scripps Institution of Oceanography, 2020; https://www.esrl.noaa.gov/gmd/ccgg/trends/gr.html). [the easiest access to this source is via the URL]

33. T. Extier *et al.*, On the use of $\delta^{18}O_{atm}$ for ice core dating. *Quat. Sci. Rev.* **185**, 244-257 (2018).

34. L. Bazin *et al.*, An optimized multi-proxy, multi-site Antarctic ice and gas orbital chronology (AICC2012): 120-800 ka. *Clim. Past* **9**, 1715-1731 (2013).

35. H. Cheng *et al.*, The Asian monsoon over the past 640,000 years and ice age terminations. *Nature* **534**, 640-646 (2016).

36. A. Bozbiyik, M. Steinacher, F. Joos, T. F. Stocker, L. Menviel, Fingerprints of changes in the terrestrial carbon cycle in response to large reorganizations in ocean circulation. *Clim. Past* **7**, 319-338 (2011).

37. R. M. Spratt, L. E. Lisiecki, A Late Pleistocene sea level stack. *Clim. Past* **12**, 1079-1092 (2016).

38. S. Barker *et al.*, Icebergs not the trigger for North Atlantic cold events. *Nature* **520**, 333-336 (2015).

39. A. J. Dickson *et al.*, Oceanic forcing of the Marine Isotope Stage 11 interglacial. *Nat. Geosci.* **2**, 428-433 (2009).

40. R. G. Hatfield *et al.*, Interglacial responses of the southern Greenland ice sheet over the last 430,000 years determined using particle-size specific magnetic and isotopic tracers. *Earth Planet. Sci. Lett.* **454**, 225-236 (2016).

41. D. J. Wilson *et al.*, Ice loss from the East Antarctic ice sheet during late Pleistocene interglacials. *Nature* **561**, 383-386 (2018).

42. J. B. Pedro *et al.*, Beyond the bipolar seesaw: Toward a process understanding of interhemispheric coupling. *Quat. Sci. Rev.* **192**, 27-46 (2018).

43. T. Chen *et al.*, Synchronous centennial abrupt events in the ocean and atmosphere during the last deglaciation. *Science* **349**, 1537-1541 (2015).

44. S. L. Jaccard, E. D. Galbraith, A. Martinez-Garcia, R. F. Anderson, Covariation of deep Southern Ocean oxygenation and atmospheric CO_2 through the last ice age. *Nature* **530**, 207-210 (2016).

45. C. Basak *et al.*, Breakup of last glacial deep stratification in the South Pacific. *Science* **359**, 900 (2018).

46. B. B. Stephens, R. F. Keeling, The influence of Antarctic sea ice on glacial–interglacial CO_2 variations. *Nature* **404**, 171-174 (2000).

47. A. Schmittner, E. D. Galbraith, Glacial greenhouse-gas fluctuations controlled by ocean circulation changes. *Nature* **456**, 373-376 (2008).

48. M. Lacerra, D. Lund, J. Yu, A. Schmittner, Carbon storage in the mid-depth Atlantic during millennial-scale climate events. *Paleoceanography* **32**, 780-795 (2017).

49. L. Menviel *et al.*, Southern Hemisphere westerlies as a driver of the early deglacial atmospheric CO_2 rise. *Nat. Commun.* **9**, 2503 (2018).

50. J. W. B. Rae *et al.*, CO_2 storage and release in the deep Southern Ocean on millennial to centennial timescales. *Nature* **562**, 569-573 (2018).

51. P. Köhler, G. Knorr, E. Bard, Permafrost thawing as a possible source of abrupt carbon release at the onset of the Bølling/Allerød. *Nat. Commun.* **5**, 5520 (2014).

52. A. Jeltsch-Thömmes, F. Joos, Modeling the evolution of pulse-like perturbations in atmospheric carbon and carbon isotopes: the role of weathering–sedimentation imbalances. *Clim. Past* **16**, 423-451 (2020).

53. C. Buizert *et al.*, Abrupt ice-age shifts in southern westerly winds and Antarctic climate forced from the north. *Nature* **563**, 681-685 (2018).

54. P. U. Clark *et al.*, Consequences of twenty-first-century policy for multi-millennial climate and sea-level change. *Nat Clim Change* **6**, 360-369 (2016).

55. B. Bereiter, T. F. Stocker, H. Fischer, A centrifugal ice microtome for measurements of atmospheric CO_2 on air trapped in polar ice cores. *Atmos. Meas. Tech.* **6**, 251-262 (2013).

56. P. P. Tans, A. M. Crotwell, K. W. Thoning, Abundances of isotopologues and calibration of CO_2 greenhouse gas measurements. *Atmos. Meas. Tech.* **10**, 2669-2685 (2017).

57. H. Schaefer *et al.*, On the suitability of partially clathrated ice for analysis of concentration and $\delta^{13}C$ of palaeo-atmospheric CO_2. *Earth Planet. Sci. Lett.* **307**, 334-340 (2011).

58. A. Schilt *et al.*, Glacial–interglacial and millennial-scale variations in the atmospheric nitrous oxide concentration during the last 800,000 years. *Quat. Sci. Rev.* **29**, 182-192 (2010).

59. R. Spahni *et al.*, Atmospheric methane and nitrous oxide of the late Pleistocene from Antarctic ice cores. *Science* **310**, 1317-1321 (2005).

60. M. Bock *et al.*, Glacial/interglacial wetland, biomass burning, and geologic methane emissions constrained by dual stable isotopic CH_4 ice core records. *Proc. Natl. Acad. Sci. U.S.A.* **114**, E5778-E5786 (2017).

61. D. Hodell *et al.*, A reference time scale for Site U1385 (Shackleton Site) on the SW Iberian Margin. *Glob. Planet Change* **133**, 49-64 (2015).

62. N. J. Shackleton, R. G. Fairbanks, T.-C. Chiu, F. Parrenin, Absolute calibration of the Greenland time scale: implications for Antarctic time scales and for $\Delta^{14}C$. *Quat. Sci. Rev.* **23**, 1513-1522 (2004).

63. B. Martrat *et al.*, Four climate cycles of recurring deep and surface water destabilizations on the Iberian Margin. *Science* **317**, 502-507 (2007).

64. L. C. Skinner, H. Elderfield, Rapid fluctuations in the deep North Atlantic heat budget during the last glacial period. *Paleoceanography* **22**, PA1205 (2007).

65. P. C. Tzedakis, K. H. Roucoux, L. de Abreu, N. J. Shackleton, The duration of forest stages in southern Europe and interglacial climate variability. *Science* **306**, 2231-2235 (2004).

66. S. Barker *et al.*, 800,000 years of abrupt climate variability. *Science* **334**, 347-351 (2011).

67. H. Craig, Y. Horibe, T. Sowers, Gravitational separation of gases and isotopes in polar ice caps. *Science* **242**, 1675-1678 (1988).

68. T. Sowers, M. Bender, D. Raynaud, Elemental and isotopic composition of occluded O_2 and N_2 in polar ice. *J. Geophys. Res.* **94**, 5137-5150 (1989).

69. D. M. Etheridge *et al.*, Natural and anthropogenic changes in atmospheric CO_2 over the last 1000 years from air in Antarctic ice and firn. *J. Geophys. Res.-Atmos.* **101**, 4115-4128 (1996).

70. S. Eggleston, J. Schmitt, B. Bereiter, R. Schneider, H. Fischer, Evolution of the stable carbon isotope composition of atmospheric CO_2 over the last glacial cycle. *Paleoceanography* **31**, 434-452 (2016).

71. G. B. Dreyfus *et al.*, Firn processes and $\delta^{15}N$: potential for a gas-phase climate proxy. *Quat. Sci. Rev.* **29**, 28-42 (2010).

72. M. L. Bender, Orbital tuning chronology for the Vostok climate record supported by trapped gas composition. *Earth Planet. Sci. Lett.* **204**, 275-289 (2002).

73. B. Bereiter *et al.*, Revision of the EPICA Dome C CO_2 record from 800 to 600kyr before present. *Geophys. Res.* **42**, 542-549 (2015).

74. P. Köhler, C. Nehrbass-Ahles, J. Schmitt, T. F. Stocker, H. Fischer, A 156 kyr smoothed history of the atmospheric greenhouse gases CO_2, CH_4, and N_2O and their radiative forcing. *Earth Syst. Sci. Data* **9**, 363-387 (2017).

75. I. G. Enting, On the use of smoothing splines to filter CO_2 data. *J. Geophys. Res.-Atmos.* **92**, 10977-10984 (1987).

76. J. Schwander, B. Stauffer, Age difference between polar ice and the air trapped in its bubbles. *Nature* **311**, 45 (1984).

77. R. Spahni *et al.*, The attenuation of fast atmospheric CH_4 variations recorded in polar ice cores. *Geophys. Res.* **30**, 1571 (2003).

78. C. Buizert *et al.*, Gas transport in firn: multiple-tracer characterisation and model intercomparison for NEEM, Northern Greenland. *Atmos. Chem. Phys.* **12**, 4259-4277 (2012).

79. P. Köhler, G. Knorr, D. Buiron, A. Lourantou, J. Chappellaz, Abrupt rise in atmospheric CO_2 at the onset of the Bølling/Allerød: in-situ ice core data versus true atmospheric signals. *Clim. Past* **7**, 473-486 (2011).

80. K. Fourteau *et al.*, Analytical constraints on layered gas trapping and smoothing of atmospheric variability in ice under low-accumulation conditions. *Clim. Past* **13**, 1815-1830 (2017).

81. R. H. Rhodes *et al.*, Local artifacts in ice core methane records caused by layered bubble trapping and in situ production: a multi-site investigation. *Clim. Past* **12**, 1061-1077 (2016).

82. S. Bihorel, M. Baudin, “R Port of the 'Scilab' Neldermead Module” (Version 1.0-11, 2018; https://cran.r-project.org/web/packages/neldermead/neldermead.pdf). [the easiest access to this source is via the URL]

83. F. Parrenin *et al.*, Synchronous change of atmospheric CO_2 and Antarctic temperature during the last deglacial warming. *Science* **339**, 1060-1063 (2013).

84. C. Buizert *et al.*, The WAIS Divide deep ice core WD2014 chronology - Part 1: Methane synchronization (68-31 kaBP) and the gas age-ice age difference. *Clim. Past* **11**, 153-173 (2015).

85. D. York, Least-squares fitting of a straight line. *Can. J. Phys.* **44**, 1079-1086 (1966).

86. D. Lüthi *et al.*, CO_2 and O_2/N_2 variations in and just below the bubble–clathrate transformation zone of Antarctic ice cores. *Earth Planet. Sci. Lett.* **297**, 226-233 (2010).

Acknowledgments: The authors thank M. Häberli, O. Eicher, S. Eggleston, C. Bréant, J. Beck, and B. Seth for assistance with sample acquisition. We acknowledge the support of G. Aufresne who conducted additional CH_4 measurements at IGE. Samples from Site U1385 were provided by the International Ocean Discovery Program (IODP). J. Booth, S. Crowhurst, J. Nicolson, J. Rolfe, and M. Mleneck-Vautravers are thanked for laboratory support. Thanks to R. Walther, S. Marending, K. Grossenbacher, H.P. Moret, and R. Bleisch for technical assistance and E. Brook for helpful comments on an earlier version of the manuscript. **Funding:** This work is a contribution to the “European Project for Ice Coring in Antarctica” (EPICA), a joint European Science Foundation/European Commission scientific program, funded by the European Union and by national contributions from Belgium, Denmark, France, Germany, Italy, The Netherlands, Norway, Sweden, Switzerland, and the United Kingdom. The main logistic support was provided by IPEV and PNRA. This is

EPICA publication no. ###. C.N., J. Schmitt, B.B., F.J., A.S., L. Schmidely, L.Silva, H.F., and T.F.S. acknowledge long-term financial support by the Swiss National Science Foundation (SNF project numbers #200020_159563, #200020_172745, #200020_172506, #200020_172476, and #20FI21_189533). This project is TiPES contribution ###: This project has received funding from the European Union's Horizon 2020 research and innovation program under grant agreement #820970. **Author contributions:** C.N., J. Schmitt, B.B., J.C., D.H., H.F., and T.F.S. designed the research. C.N. performed the measurements with contributions from J. Shin, A.S., G.T, and R.G.. Data analyses were led by C.N. with contributions from J. Schmitt, B.B., F.J., L. Schmidely, L. Silva, D.H., H.F., and T.F.S.. C.N. and T.F.S. led the writing of the manuscript with inputs from all authors. **Competing interests:** The authors declare no competing interests. **Data and materials availability:** All data are available online in the supplementary materials and through the PANGAEA data depository (https://doi.org/10.1594/PANGAEA.915146).

Supplementary Materials:

Materials and Methods
Supplementary text
Figures S1-S9
Table S1
References (*55-86*)
Data S1-S2

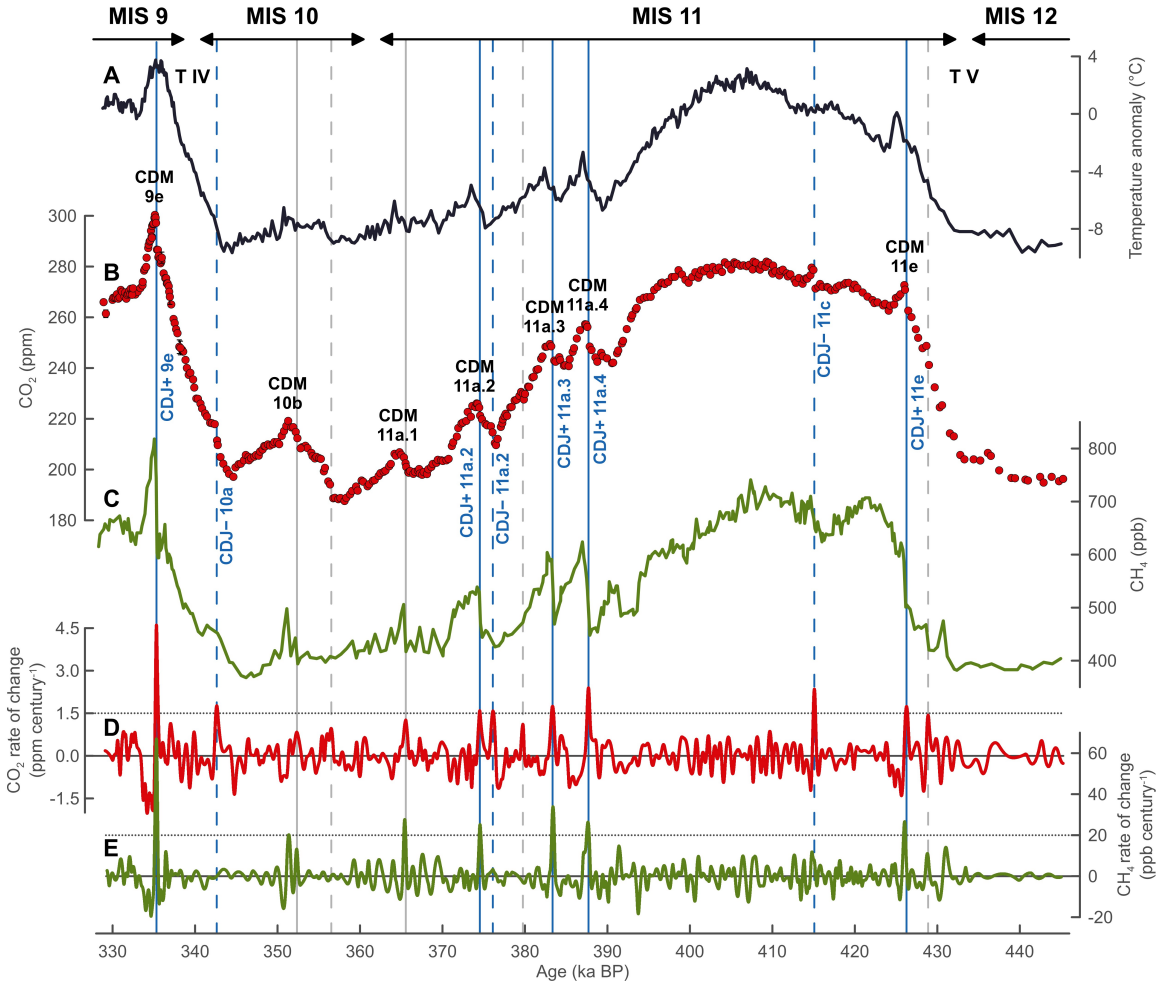

Fig. 1. High-resolution CO_2 and improved CH_4 records compared to Antarctic temperature during MIS 9e - 12a. (**A**) Antarctic temperature anomalies (*10*). (**B**) CO_2 record (this study). (**C**) CH_4 compilation [this study, (*20*)]. (**D**) Rate of change of CO_2 in the ice core record derived from (B) (*20*). (**E**) Rate of change of CH_4 in the ice core record derived from (C) (*20*). All data are based on measurements of EDC ice core samples and are plotted on the AICC2012 age scale (*34*). Identified CDM and CDJ are labelled according to the MIS assignment by Ref. (*19*). Distinct CDJ in the CO_2 record are highlighted by blue vertical lines, positioned at the peaks in (D) exceeding a threshold value of 1.5 ppm per century (*20*). CDJ+ (solid lines) coincide with major CH_4 rises greater 50 ppb at growth rates greater than 20 ppb per century (E), while CDJ− (dashed lines) do not. Further potential events with positive rates below 1.5 ppm per century (D) are not labelled but marked by grey vertical lines.

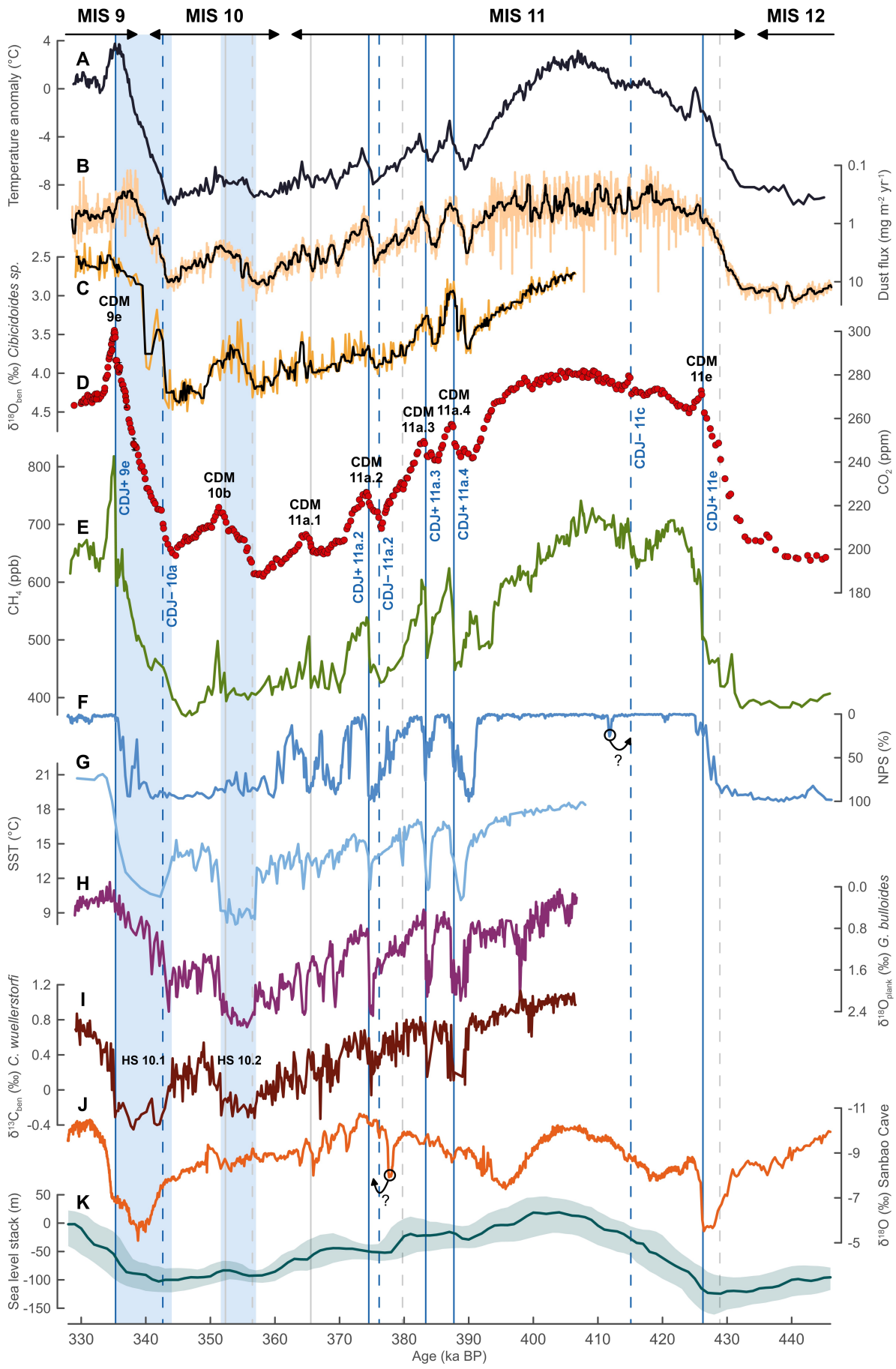
MIS 9
MIS 10
MIS 11
MIS 12
A
B
C
D
E
F
G
H
I
J
K
Temperature anomaly (°C)
Dust flux (mg m⁻² yr⁻¹)
δ18Oben (‰) Cibicidoides sp.
CO2 (ppm)
CH4 (ppb)
NPS (%)
SST (°C)
δ18Oplank (‰) G. bulloides
δ13Cben (‰) C. wuellerstorfi
δ18O (‰) Sanbao Cave
Sea level stack (m)
Age (ka BP)
CDM 9e
CDM 10b
CDM 11a.1
CDM 11a.2
CDM 11a.3
CDM 11a.4
CDM 11e
CDJ+ 9e
CDJ− 10a
CDJ+ 11a.2
CDJ− 11a.2
CDJ+ 11a.3
CDJ+ 11a.4
CDJ− 11c
CDJ+ 11e
HS 10.1
HS 10.2

Fig. 2. Comparison of high-resolution CO_2 and improved CH_4 records with marine sediment and speleothem data covering MIS 9e - 12a. (**A**) EDC temperature anomalies (*10*). (**B**) EDC dust flux (*27*), including a ~500 year running median. (**C**) Benthic $\delta^{18}O$ *C. wuellerstorfi* from IODP Site U1385 on the Iberian Margin (this study), including a ~500 year running median. (**D**) EDC CO_2 record (this study). (**E**) EDC CH_4 compilation [this study, (*20*)]. (**F**) Relative proportion of the polar planktic foraminifera *N. pachyderma* from ODP Site 983 (*38*). (**G**) $U^{k'}_{37}$ based SST from IODP Site U1385 (*26*). (**H**) Planktic $\delta^{18}O$ *G. bulloides* from IODP Site U1385 (this study). (**I**) Benthic $\delta^{13}C$ *C. wuellerstorfi* from IODP Site U1385 (this study). (**J**) $\delta^{18}O$ Sanbao Cave record in Hubei, China (*35*). (**K**) Global sea level stack (probability maximum) including 95% probability intervals (*37*). All records are given on the AICC2012 age scale (*34*) or are transferred to AICC2012 (*20*), with the exception of (J) and (K). Arrows in (F) and (J) highlight potential age scale inconsistencies. Labelling and vertical lines are identical to Fig. 1. Blue bands indicate HS 10.1 and HS 10.2 (see text for details).

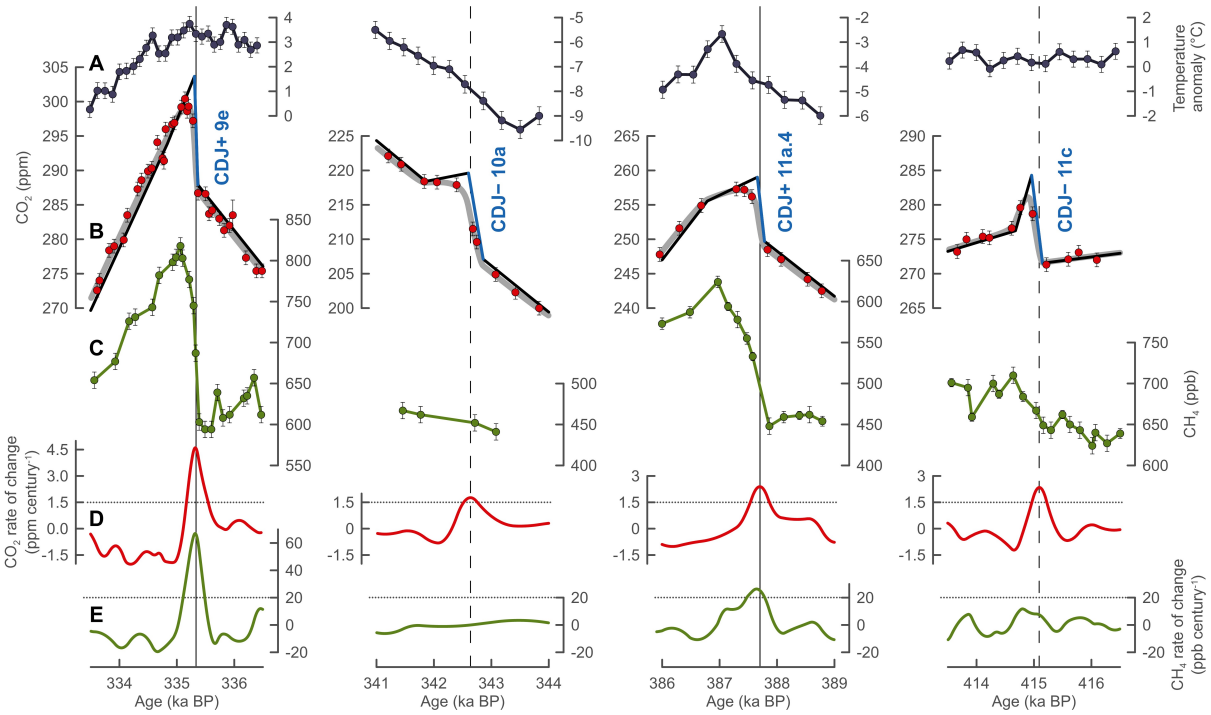

Fig. 3. Detailed view of the two varieties of CDJ. (**A-E**) Identical to Fig. 1. The black linear segments in (B) indicate first-order approximations of the atmospheric CO_2 evolution. The blue segment highlights the actual CDJ event. These approximations for the atmospheric trajectories are optimized, so that the CO_2 curve after smoothing by the bubble enclosure process (grey lines) fit the ice core data (red dots) best. The firn smoothing is realized applying new gas enclosure characteristics for the EDC ice core (*20*). See Table S1 for details. All remaining CDJ are shown in Fig. S1.

Supplementary Materials for

Abrupt CO_2 Release to the Atmosphere under Glacial and Early Interglacial Climate Conditions

C. Nehrbass-Ahles, J. Shin, J. Schmitt, B. Bereiter, F. Joos, A. Schilt, L. Schmidely, L. Silva, G. Teste, R. Grilli, J. Chappellaz, D. Hodell, H. Fischer, and T. F. Stocker.

correspondence to: cn425@cam.ac.uk

This PDF file includes:

Materials and Methods
Supplementary Text
Figs. S1 to S9
Table S1
Captions for Data S1 to S2
References (*55-86*)

Other Supplementary Materials for this manuscript includes the following:

Data S1 to S2

Materials and Methods

EPICA Dome C CO_2 measurements

The majority of CO_2 measurements on the EPICA Dome C (EDC) ice core were performed at Climate and Environmental Physics (CEP), Physics Institute, University of Bern, Switzerland. The data were measured using the recently developed dry-extraction system, the Centrifugal Ice Microtome (CIM), described in detail in Ref. (*55*). With this friction-free extraction system, we performed a total of 1161 single measurements with a polar ice sample throughput of up to 24 samples per day. On average, individual ice samples weighed 7.3±0.8 g after approximately 5 mm was trimmed from the outer surfaces. Additionally, we performed 463 control measurements throughout the measurement campaign to correct offsets related to the extraction process and to monitor potential system drifts. These measurements involve expanding a standard gas over a gas-free ice sample that is treated identically to a polar ice sample, and is measured against the same calibration gas (*55*). Typically, we made one control measurement for every four polar ice samples amounting to five to seven control measurements per measurement day. Over the course of the measurement campaign, which was approximately one year, the mean control measurement was 2.31±1.21 ppm higher than the calibrated value of the reference gas that has been mixed over the gas-free ice. All polar ice measurements have been corrected using the daily average of these control measurements.

All individual depth levels were measured at least in duplicate. For approximately 50% of all samples, a set of vertically contiguous (i.e., directly neighboring) replicate measurements were performed on a different day, leading to a mean sample replication of three samples per final data point. All CIM measurements were grouped (i.e., averaged) to depth sections of usually ~5 cm (in rare cases up to 12 cm) in the vertical direction, thereby integrating the signal on average over 23±7 years until 425 ka BP (thousand years before present, where present is defined as 1950 CE), and 60±16 years beyond. In total we provide 387 new data points between 330 and 450 ka BP [i.e., Marine Isotope Stage (MIS) 9e - 12a]. The pooled standard deviation for all replicate samples is 1.0 ppm, which is used as an error estimate for all CIM measurements. All CIM CO_2 measurements are referenced to the WMOX2007 mole fraction scale (*56*) using four different primary dry air standards calibrated at the NOAA Earth System Research Laboratory, Boulder, USA ranging between 192.44±0.11 and 363.08±0.06 ppm CO_2.

An additional 33 measurements between 297 and 353 ka BP were performed at the Institut des Géosciences de l'Environnement (IGE), Univ. Grenoble Alpes, France using the Ball Mill extraction technique described in detail in Ref. (*57*). Here, larger samples of 42.5±2.5 g were used. The extracted air of each sample is analyzed five consecutive times (i.e., in total five sample injections into the gas analyzer). The precision of the system amounts to an average of ~1.7 ppm and is based on the standard deviation of these five injections, thus does not include the additional extraction variability of replicate samples. The CO_2 measurements are calibrated using a working standard (233.7±0.4 ppm CO_2, synthetic dry air provided by Air Liquide, Grenoble, France), which has been referenced to two primary dry air standards with calibrated CO_2 mole fractions of 238.34±0.04 ppm and 260.26±0.20 ppm, provided by the NOAA Earth System Research Laboratory, Boulder, USA and the Commonwealth Scientific and Industrial Research Organisation (CSIRO), Australia, respectively.

Gas ages for all CO_2 measurements produced by the CIM and Ball Mill were calculated using the average depth levels of each depth section using the AICC2012 chronology (*34*). We do not find any significant inter-laboratory offset; however, this comparison is only based on 11 directly neighboring samples. Note that due to their lower temporal resolution, the Ball Mill data younger than 328 ka BP are not shown in Fig. 1B and Fig. 2D. All CO_2 data are available in Data S1.

EPICA Dome C CH_4 measurements and compilation of CH_4 data

The existing CH_4 record for MIS 9e - 12a consists of measurements from two experimental setups, one employed at CEP, the other at IGE (*21*). Here we improve the temporal resolution using the same experimental setups. A total of 92 unpublished CH_4 data points had been produced in 2008 using the CEP setup, within the scope of the work by Ref. (*58*), but remained unpublished. The method used for these samples is identical to that described in Ref. (*21*). Secondly, we performed 41 new measurements at IGE at time periods of abrupt climate change connected to Carbon Dioxide Jump (CDJ) events in the CO_2 record. In previous publications, an offset correction between the IGE and CEP setups involved adding 6 ppb to the IGE data (*59*). This correction is obsolete for the new IGE data as an improved contamination correction has been introduced, removing the interlaboratory offset. Lastly, we complement the above described data with 54 published data points by Ref. (*60*), that have been measured at CEP; however, with an independent setup. A visual overview of this data can be found in Fig. S2. All CH_4 data are available in Data S1.

The majority of the 92 CH_4 data points produced by Ref. (*58*) are vertically contiguous (i.e., directly neighboring) to those published by Ref. (*21*) and should be considered replicate measurements. In our CH_4 compilation (Data S1), we combine two individual measurements to one data point in cases where the vertical depth difference between two neighboring CH_4 data points is smaller than 10 cm (typically less than 5 cm). This entails a CH_4 signal integration over 28±14 years on average, which is less than the smoothing resulting from the firn column (see below). The uncertainty of these averaged values is calculated using Gaussian error propagation. We use this CH_4 compilation in all figures showing EDC CH_4 data in MIS 9e - 12a, with the exception of Fig. S2B where the full data set is shown.

Ocean sediment data from IODP Site U1385 (Shackleton site, Iberian Margin)

Isotope data from the International Ocean Discovery Program (IODP) Site U1385 between 329 and 407 ka BP were measured on the planktic foraminifera *G. bulloides* (Fig. 2H) and epibenthic species belonging to the genus *Cibicidoides* (Fig. 2C, 2I). A condensed section or hiatus in the sedimentation rate in older sections covering MIS 11c - e prevents us from reconstructing hydrographic changes on centennial time scales (*61*). Most analyses were made on *C. wuellerstorfi* but when this species was rare, other species were used for benthic $\delta^{18}O$ (i.e., *C. mundulus*, *C. robertsonianus*) (Fig. 2C). Only *C. wuellerstorfi* data are presented for benthic $\delta^{13}C$ (Fig. 2I) because other species may live infaunally and therefore do not record the $\delta^{13}C$ signal of the bottom water. All measurements were made at the Godwin Laboratory of Palaeoclimate Research, University of Cambridge, UK using the same methods as those described in Ref. (*61*). All marine sediment data are available in Data S2.

Piston cores from the Iberian Margin off Portugal contain clear signals of millennial variability of both surface and deep-water masses (*28, 62*). Variations in planktic $\delta^{18}O$ and alkenone saturation index ($U^{k'}_{37}$) reflect the temperature variations in Greenland over the last glacial cycle (*63*). In the same sediment core, the benthic $\delta^{18}O$ signal resembles the δD record in Antarctica ice cores (*28, 62*) capturing each of the Antarctic Isotope Maxima events during the last glaciation (*10*). Millennial variations in benthic $\delta^{18}O$ are affected by changes in deep-water temperature and water mass hydrography, and are assumed to be a signal that originates from the Southern Ocean (SO) (*28, 64*). We synchronized IODP Site U1385 with EDC on the AICC2012 age scale (*34*) by correlating the benthic $\delta^{18}O$ and δD records (Fig. 2C, 2A) (cf. *65, 66*). This correlation results in agreement between the planktic $\delta^{18}O$ record and the CH_4 compilation (Fig. 2H, 2E). The observed phasing of the planktic and benthic $\delta^{18}O$ signals at IODP Site U1385 is consistent with the relative changes in temperature between Antarctica and Greenland deduced from CH_4 synchronization.

Gravitational correction of the CO_2 and CH_4 data

Before small samples of the atmosphere become trapped in the ice, the air first needs to diffuse through the firn column of a polar ice sheet. Under the influence of the Earth's gravitational field heavier molecules become enriched compared to the air that entered the firn at the surface of the ice sheet (*67*), while lighter molecules become depleted. This process is commonly referred to as gravitational settling. The magnitude of this effect is dependent on the thickness of the diffusive firn column and therefore varies with changing temperature and accumulation rates. Atmospheric $\delta^{15}N_2$ (the isotopic signal of N_2) can be safely assumed to be constant over orbital time scales, which makes the $\delta^{15}N_2$ of the air trapped in the ice an ideal tracer of gravitational effects and can also be used to correct for other gas species that are subject to change in the atmosphere, such as CO_2 and CH_4 (*68, 69*).

With approximately 44 g mol^{-1} CO_2 is heavier than the mean molar weight of air, which amounts to 29 g mol^{-1} causing slightly higher CO_2 mole fractions where bubble formation takes place. With 16 g mol^{-1} CH_4 is lighter than air leading to slightly lower CH_4 mole fractions at bubble close off. While the correction of such effects is vital for reconstructions of stable isotopic ratios (e.g., *29*), it was not systematically corrected for in previous studies solely focusing on mole fractions, as the effect is only on the order of 1% of the measured value.

Although this systematic bias is well known, many authors refrained from applying this correction, possibly due to the lack of $\delta^{15}N_2$ data (or similar proxies) or the generally small magnitude of the correction which often was smaller than the measurement precision. However, with steadily increasing technical capabilities and a growing body of $\delta^{15}N_2$ data the above raised arguments are obsolete. In particular, with respect to the accumulating evidence for systematic non-trivial offsets between different CO_2 reconstructions this correction is necessary (*4, 70*).

To estimate the gravitational correction for EDC data, we use $\delta^{15}N_2$ measurements published by Ref. (*71*). For each of our data points, we find the corresponding EDC δD value by linear approximation of the δD data set published by Ref. (*10*). Subsequently, we make use of the linear relationship between δD and $\delta^{15}N_2$ to approximate our $\delta^{15}N_2$ as previously proposed by Ref. (*29*). The Vostok data shown in Fig. S2A are corrected using a linear regression between δD (*10*) and $\delta^{15}N_2$ (*72*). The additional error introduced by this correction is negligible compared to the experimental errors of the CO_2 mole fractions. The gravitational correction for our measurements involves reducing the uncorrected CO_2 data by 1.1 to 2.5 ppm and adding between 2 and 6 ppb to the CH_4 data.

Note that all CO_2 and CH_4 values shown in Fig. 1, 2, 3, S1, and S2 are corrected for gravitational effects. In order to provide CO_2 mole fractions that are consistent with previously published CO_2 compilations where gravitational corrections have not been consistently applied (*73, 74*), we also provide uncorrected CO_2 and CH_4 data in Data S1.

Calculating the rate of CO_2 and CH_4 change in the ice core record

To calculate rate of change in CO_2 (Fig. 1D) on centennial to millennial timescales, superimposed orbital trends have to be removed from the data set first (cf. *66*). This is achieved by subtracting a smoothing spline from the data set (*75*), with cut-off periods (i.e., degrees of smoothing) ranging from 6 to 14 ka (Fig. S3A). Subsequently, we use a second set of smoothing splines with cut-off periods ranging from 0.4 to 1.2 ka to interpolate these detrended data to obtain annually resolved equidistant records (Fig. S3B - F). These interpolated data are used to calculate central finite differences to approximate the first derivative of these CO_2 records (Fig. S3G - K). For the removal of orbital scale variability, we choose the 10 ka cut-off period smoothing function, which is a compromise between preserving sub-millennial scale variability while removing the orbital-scale glacial-interglacial trends. The interpolation of the detrended data is done using a 0.8 ka cut-off period smoothing function, which is a compromise

between the amplification of high-frequency noise and loss of signal amplitude of potential CDJ events (cf. *66*). The same methodology is used for calculating the rate of change in the CH_4 record (Fig. 1E).

Estimating realistic Gas Age Distributions for the EDC ice core

The air trapped at a particular depth of the ice core is a mixture over decades to millennia depending on accumulation rate and site temperature (*76*). The atmospheric air diffuses through the firn column and mixes with older air masses before it gets trapped in the ice. Most importantly, bubbles in the firn-ice transition (lock-in) zone close off slowly and not at the same time which leads to an attenuation or low-pass filtering of the atmospheric signal (*77, 78*). This process scales with the time it takes a single layer of firn/ice to pass through the lock-in zone. The age difference (delta age) between the ice and the mean age of the gas trapped within the ice is a first-order indicator of average accumulation rates over the entire firn column. With decreasing accumulation these effects become more pronounced, leading to a particularly strong signal attenuation and multi-millennial delta ages in the Vostok and EDC ice core that are from low-accumulation sites located on the Antarctic Plateau. The age of the enclosed air after this firn column-induced smoothing is described by a probability density function. It is often referred to as the Gas Age Distribution (GAD), and its width is different for each depth section depending on past accumulation rates and temperatures. Figure S4 shows three typical shapes (blue lines) of commonly used GAD for the EDC ice core (*77, 79*), two of which are representative for warm interglacial (pre-industrial) and cold glacial conditions (Last Glacial Maximum), respectively.

Recently, Ref. (*80*) described an empirical method to estimate GAD for the Vostok ice core based on the direct comparison between continuously measured CH_4 records. This method involves finding a generic GAD that convolves the high-frequency CH_4 signal captured by the West Antarctic Ice Sheet Divide (WD) ice core (*18*) at points of fast CH_4 transitions (in their case DO 17 at ~59 ka BP) to match the smoothed version of the identical atmospheric signal in the Vostok ice core. The assumption is made that the continuous WD CH_4 record provides an insignificantly smoothed version of the atmospheric signal (*6*). Ref. (*80*) raised concern that commonly used modelled estimates of GAD for low-accumulation sites during glacial conditions may be systematically too wide. Consequently, such GAD would lead to a systematic overestimation of the firn column-induced smoothing effect. However, it is yet unknown whether this finding is unique to the Vostok ice core under glacial conditions or whether interglacial GAD estimates are affected in a similar way. Moreover, it is not clear – although likely – whether this applies to other ice cores with similar temperature and accumulation regimes, such as the EDC ice core.

Indirect evidence that commonly used GAD for the EDC ice core (*77*) are too wide comes from a study by Ref. (*79*). They estimated the atmospheric CO_2 rise rates for the CDJ+ found at the onset of the Bølling-Allerød (BA) period (*9*) using a GAD similar to that predicted by Ref. (*77*) (Fig. S4). By comparison with the WD CO_2 record, their estimations were later shown to be clear overestimations of the atmospheric rise rates (*6*), which can be explained by the usage of a too wide GAD in the study by Ref. (*79*).

Following the techniques described in Ref. (*80*), it is possible to test the commonly used modelled GAD (*77*) in the case of the EDC ice core. The WD CH_4 record is available at decadal resolution for the period between 10 and 67 ka BP (*18*), where only discretely measured data are available from the EDC ice core (*21*). In comparison to a continuous record, this record is much lower in resolution (approx. 160 years between 10 and 67 ka BP on average) and suffers from staggered layering artefacts (centimeter-scale age scale reversions) that cannot be unambiguously identified in a non-continuous record (*80, 81*). Furthermore, all measurements

over MIS 3 predating ~30 ka BP are located in the brittle ice zone of the EDC ice core, which is prone to sample contamination by drilling fluid and modern air.

Nevertheless, the discrete EDC CH_4 data are sufficient to construct a first-order approximation of a more realistic GAD. Here, we focus on the onsets of three key periods that are associated with fast atmospheric CH_4 rises, namely the Preboral (PB), Younger Dryas (YD), and the BA. In addition, we also include Dansgaard-Oeschger (DO) events 6 - 8 between 33 and 39 ka BP (Fig. S5) associated with a major CH_4 rise for each DO event. Together with the data available for the last deglaciation (10 to 22 ka BP), this interval has the highest temporal resolution (~100 years) in the 10 to 67 ka BP interval where continuous WD CH_4 data are available (*18*). We assume that the GAD can be approximated by log-normal distributions (*79, 80*) and that a single GAD is representative for the enclosure characteristics for these events. Log-normal functions are described by two free parameters: the mean (μ) and standard deviation (σ) of the logarithm. For the sake of simplicity, we fix the standard deviation at a value of σ=1.5 (*80*) and vary only the mean to change the shape of our GAD. We also report the arithmetic mean of the log-normal function [referred to as expected mean in Ref. (*79*)] representing the width of the GAD, given in years (Table S1). The arithmetic mean of a log-normal distribution is given by

$$GAD_{mean} = e^{\mu+0.5\sigma^2}. \quad \text{Eq. S1}$$

We use the *fminbnd* function of the 'neldermead' package in R (*82*) to optimize the EDC bubble enclosure characteristics by smoothing the WD CH_4 data (*18*) to fit the EDC data (*21*). The optimal GAD is determined by minimizing the root-mean-square error (RMSE) between the convoluted WD CH_4 signal and the discrete EDC data, spanning a 2 ka time window centered around the inflection point of the abrupt CH_4 rise in the EDC record (Fig. S5). We allow for linear adjustments of the discrete EDC data relative to the continuous WD CH_4 data to compensate for the temporal shift induced by the convolution of the WD CH_4 signal (*79*), as well as general age scale and standardization inconsistencies. To acknowledge the dependency on the absolute value of individual data points we apply a Monte Carlo type approach and vary the discrete CH_4 data within their uncertainty boundaries (±10 ppb) in a random manner. We use the average of 500 iterations to determine the most suitable GAD width for each event. In this context the choice of age scale is critical, as it has a strong influence on the duration of an event. Therefore, we use the age scale as published by Ref. (*83*) that has been specifically optimized for the deglaciation period and includes the PB, YD, and BA events. Note that for all other purposes the AICC2012 age scale is used (*34*). For the glacial GAD – as represented by DO 6 - 8 between 33 and 39 ka BP – a longer time window is chosen for the optimization to compensate for the influence of age scale inconsistencies between the AICC2012 (discrete EDC CH_4 data) (*34*) and the WD2014 age scale (continuous WD CH_4 data) (*84*) and minimize the influence of potential staggered layering artefacts (*18, 80*) in this section (Fig. S5).

The smoothed versions of the WD CH_4 record match the discrete EDC CH_4 data well for all three events during the deglaciation (Fig. S5). In the case of DO 6 - 8 the size of each event in the discrete EDC data is well captured by the smoothed version of the WD CH_4 record, despite obvious age scales issues, indicated by relative shifts between the discrete and smoothed continuous records. The results of this optimization (Fig. S4, S5) point towards a substantial overestimation of the smoothing produced by commonly used modelled EDC enclosure characteristics (*77*), in line with Ref. (*80*).

Since these four time periods are only representative for a given firn column condition, we strive to find a simple model that allows to estimate the GAD width (Eq. S1) for other firn column conditions at Dome C, as approximated by the delta age. Therefore, we plot the arithmetic means of the GAD found for the PB, YD, BA, and DO 6 - 8 against their respective

delta age to the nearest 0.1 ka (Fig. S6). Delta ages are derived from the AICC2012 age scale (*34*) by subtracting the assigned gas age from the respective ice age for each depth interval. We use a 2 ka time window centered around the inflection point of each event to find the corresponding average delta age given on the ice age scale. Subsequently, a linear regression model incorporating the uncertainties for both variables (*85*) is utilized to obtain the following empirical relationship:

$$GAD_{mean} = 0.048(\pm 0.025) \times delta\ age\ (in\ years) + 17(\pm 67)\ years. \quad \text{Eq. S2}$$

This linear function serves as a first-order approximation of more realistic GAD for the EDC ice core, assuming a linear scaling of the GAD width with delta age.

We stress that these GAD estimates are limited in several aspects. Most importantly, these estimates are highly dependent on the used age scale, as the duration of fast CH_4 transitions and the delta age estimate may vary considerably. Also the choice of the GAD template (here a log-normal distribution) might have an influence on the quantitative outcome of this analysis. However, the good correspondence of the WD record smoothed by a log-normal GAD with the measured EDC record strongly suggests that such an influence does not affect the overall conclusions of our study. We recommend that this case study is repeated when higher resolution data from the EDC ice core for selected time periods of fast atmospheric CH_4 change and improved empiric GAD information become available.

Inversed convolution of Carbon Dioxide Jumps

The rates of CO_2 increase archived in the ice core record during CDJ can only be interpreted as lower limits for the unfiltered atmospheric rates. Independent of the original atmospheric trajectory, the growth rates in atmospheric CO_2 must have been higher than recorded in the smoothed ice core record. It is therefore important to consider the air enclosure characteristics of the EDC ice core when attempting to deconvolute the ice core signal and estimate potential atmospheric rates.

Using our GAD estimates for the EDC ice core derived as described above, we provide first-order estimates of atmospheric duration, magnitude of the CO_2 rise, and growth rates for each event identified here. To achieve this, we assume that the centennial to millennial-scale atmospheric trajectories can be approximated by a simple set of linear functions. Our atmospheric rates are estimated following these steps: (i) Find the delta age for the CDJ using the AICC2012 age scale (*34*); (ii) determine a suitable GAD using the linear relationship described above; (iii) guess a simple atmospheric trajectory, smooth this guess using the GAD, calculate RMSE between smoothed guess and the actual CO_2 data, and optimize this atmospheric guess using the Nelder-Mead algorithm; (iv) repeat step (iii) 200 times with randomly modified CO_2 record within the measurement uncertainty (±1 ppm); (v) calculate the median values for the duration, magnitude of the CO_2 rise, and growth rates for each CDJ of these 200 iterations, as indicated by blue segments in Fig. 3B and S1B. The results are shown in Table S1, where the interquartile range of these 200 iterations is used as an error estimate.

Supplementary Text

Comparison of the new CO_2 data set with previously published records

Our new EDC CO_2 data overall agree with the published Vostok 5G measurements [Fig. S2A, (*1*)]. Differences in the two records can be explained by age scale uncertainties beyond 355 ka BP due to the lack of stratigraphic tie points in the Vostok record, leading to inconsistencies of up to ~10 ka (*33, 34*). During MIS 11c - e (~390 to 430 ka BP) our data agree well with the data published by Ref. (*2*) measured on the same ice core. No difference in average mole fractions is found; however, the precision of our new data has been increased

substantially. Towards MIS 12a our new data develops an offset with respect to the data published by Ref. (*2*). Based on the time interval between 438 and 446 ka BP, where CO_2 appears to be stable at a level of 196.2±0.7 ppm (CIM measurements), we determine an offset of 3.5±1.4 ppm between the record published by Ref. (*2*) and our new CIM data, with our data showing lower mole fractions. Such offsets between different Antarctic records are well known, but still lack a coherent explanation and responsible mechanisms are hard to distinguish from each other (*4, 70*). However, the majority of mechanisms cause the CO_2 mole fractions to increase over time, for example due to preferential loss of oxygen during storage of the samples (*4, 70*). The only known effects that lead to lower CO_2 measurements are related to the combination of measurement setups with low extraction efficiencies and ice from either the so called Bubble to Clathrate Transition Zone (*57, 86*) or from depth sections in EDC deeper than 3000 m (*73*). Both mechanisms can be excluded here. Instead, we speculate that the offset is an issue related to standardization methods. While the new data were calibrated using standard reference gases ranging between 192 and 363 ppm (see Materials and Methods), Ref. (*2*) used air standards only ranging between 252 and 342 ppm (cf. *9*), i.e., the lowest concentration standard was still about 50 ppm higher than the lowest measured ice core mole fraction during MIS 12a. In any case, this small glacial offset between the new and older EDC data from this time interval does not affect any of the conclusions drawn in our study.

Estimating the detection limit for CDJ during MIS 9e - 12a in the EPICA Dome C ice core

The absence of CDJ (according to our CDJ definition in the main text) between MIS 10a and late MIS 11a (~345 to 370 ka BP) as well as between early MIS 11e and MIS 12a (~430 to 445 ka BP) raises the question of whether no CDJ events occurred during these periods or if we are only unable to detect them.

It is possible that we do not detect potential CDJ that are smaller than a certain threshold due to the firn column-induced attenuation of the original atmospheric signal. This smoothing effect is strongest for the glacial maxima when temperatures and accumulation rates are at their lowest. Besides the amount of firn smoothing, the detection limit for CDJ in our CO_2 record also depends on the original atmospheric rates and durations of carbon releases to the atmosphere.

We simulate the resulting rate of change of CO_2 as it would be recorded in the EDC ice core (cf. Fig. 1D, 3D, S1D) by smoothing generic CDJ (i.e., simple step functions) and subsequently calculating their rate of change using the same methodology as described above (Fig. S7). We use the maximum firn column-induced smoothing in the MIS 9e - 12a interval, which is found for the glacial maximum during MIS 12a when the delta age reaches its maximum at 4.5±0.3 ka (*34*) resulting in an arithmetic mean of 233±132 years (Eq. S2) for the GAD used here.

Figure S8 demonstrates the influence of both the simulated magnitude of the CO_2 rise (rows) and event duration (columns) in the atmosphere on the estimated growth rates of a CDJ event as it would be recorded by ice core record, whereas Fig. S7 visualizes the impact of different magnitudes of the CO_2 rise at a fixed CDJ duration (Fig. S7A - C) and *vice versa* (Fig. S7D - F).

Other factors – such as sample availability – may also influence the theoretical detection limit, which can lead to the overestimation of the estimated CDJ duration and underestimation of the determined atmospheric CO_2 rise and growth rate. This may be the case for CDJ– 11a.2, CDJ+ 11a.3, and CDJ+ 11e (Fig. S1). In case of CDJ+ 11e – where we exploited all available ice in this depth section – the CH_4 data suggest a later onset of the CDJ by ~100 years (i.e., a shorter duration) than we estimate based on the inverse convolution of the ice core signal (Table S1). The low ice availability is a result of earlier sampling (e.g., *2, 21, 60*) and generally lower ice availability due to low-accumulation rates during the MIS 12a - 11e transition

(Termination V) in the EDC ice core. While the majority of our CO_2 dataset is only marginally affected by limited sample availability, we cannot exclude that potential CDJ with CO_2 rises greater than ~5 ppm remain undetected during the MIS 12a - 11e transition.

In summary, based on the above theoretical considerations we should be able to detect CDJ with an atmospheric CO_2 rises greater than ~5 ppm and a duration of less than ~250 years throughout MIS 9e - 11e, i.e., the majority of our record. The finding is supported by the identification of the third largest CDJ of all eight CDJ identified in this study (CDJ– 10.a; Table S1), which takes place among the coldest conditions during the entire MIS 10a - 11a glacial period. Consequently, CDJ– 10a is associated with more pronounced firn column-induced smoothing of the atmospheric signal as compared to the preceding MIS 10b to late MIS 11a interval (i.e., ~345 to 370 ka BP) where no CDJ are found (Fig. 1), confirming that we do capture major CDJ even when the firn column-induced signal attenuation is relatively strong.

We speculate that CDJ+ become less likely with decreasing temperatures during a glacial period based on previously published lower precision CO_2 data. We assume that at least four CDJ+ occurred during MIS 5a - c associated with DO 19 - 21 and DO 24 based on apparent jumps in the CO_2 trajectories at the time of sharp CH_4 rises (*4, 8*), but no robust conclusion can be drawn from these data. With advancing glacial conditions (i.e., decreasing temperatures and lower sea levels) towards MIS 3 the climatic conditions seem to no longer permit the formation of major CDJ+ (*4, 5, 8*). A single CDJ– associated with Heinrich Stadial (HS) 4 (*12, 13*) is the only CDJ identified for the MIS 3 interval so far, with no indications of CDJ+ associated with major Carbon Dioxide Maxima (CDM) 4, 8, 12, 14, and 17 (numbering refers to the associated DO event) (*4, 8*). With the onset of the last deglaciation connected with rising temperatures and sea level, both types of CDJ seem to become more likely again (*6, 30*). It is thus conceivable that the climatic boundary conditions found during the early glacial growth phases (e.g., MIS 11a, MIS 5a - c) are favorable conditions for the formation of CDJ+ events, that seem to cease towards the coldest conditions reached during the glacial maxima of each glacial cycle (e.g., MIS 10, MIS 3). CDJ–, on the other hand, seem to depend on specific conditions potentially triggered by major freshwater forcing.

CH_4 excursions during Heinrich Stadials in the EPICA Dome C ice core

By comparison with the CDJ− found for HS1 (*6*) and HS4 (*12*), we would expect to find simultaneous short-lived overshoots in the CH_4 record, with amplitudes of less than ~50 ppb (*18*). However, the CDJ− identified here (i.e., CDJ− 10a, 11a2, 11c) show no indication of such signals in the CH_4 data.

We argue that such events cannot be resolved with currently available discrete EDC CH_4 data. This statement is based on considerations for the known events for HS1 and HS4 (*18*), that are smoothed using our linear model for delta age dependent GAD (Fig. S9). In both cases the short-lived CH_4 overshoot is attenuated to a level that cannot be detected in the EDC ice core, at least by using the discrete CH_4 data from Ref. (*21*), due to insufficient temporal resolution and measurement precision. This is in line with Ref. (*80*), who showed that comparable sub-centennial-scale CH_4 variations around DO 17 in the WD CH_4 record are smoothed out in the Vostok ice core.

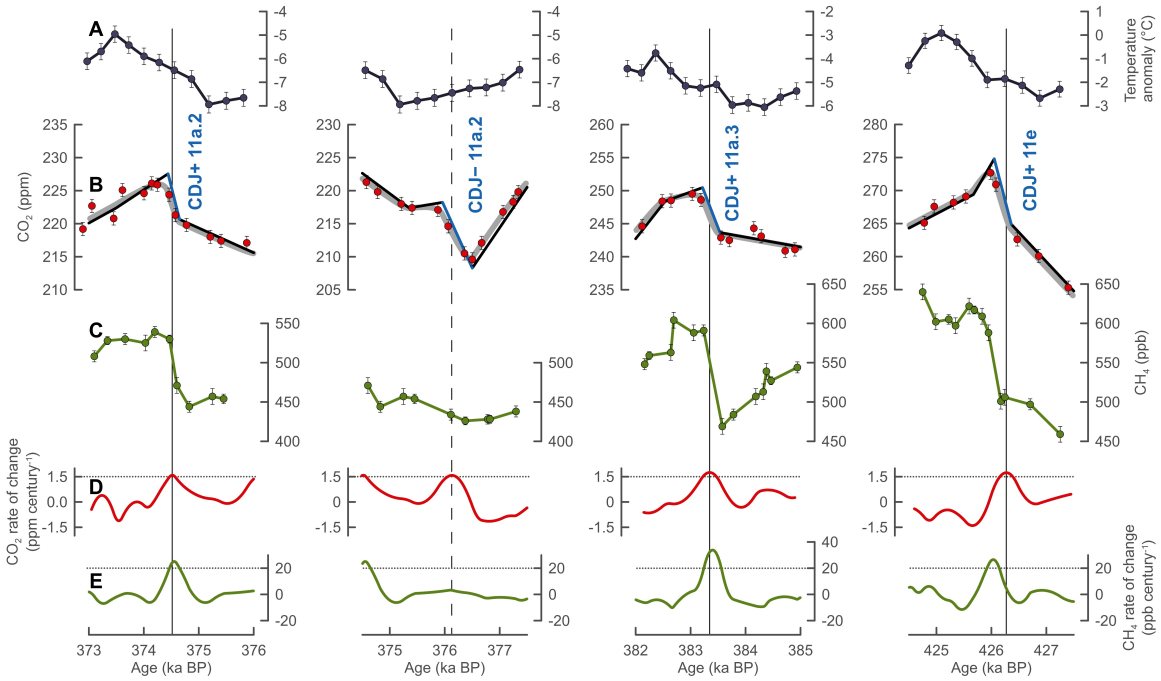

Fig. S1. Extension of Fig. 3. Detailed view of the two varieties of Carbon Dioxide Jumps (CDJ) in the EPICA Dome C (EDC) ice core. (**A**) EDC temperature anomalies (*11*) (**B**) CO_2 data (this study). (**C**) CH_4 compilation (this study, see materials and methods for details). (**D**) Rate of change in CO_2 (cf. Fig. 1D). (**E**) Rate of change in CH_4 (cf. Fig. 1E). CDJ+ are coeval with DO-like CH_4 rises greater 50 ppb at growth rates greater than 20 ppb per century (D), whereas CDJ− are not. The black linear segments in (B) indicate first-order approximations of the atmospheric CO_2 evolution. The blue segment highlights the actual CDJ event. These approximations for the atmospheric trajectories are optimized so that the CO_2 curve after smoothing by the bubble enclosure process (grey lines) fit the ice core data (red points) best. The firn smoothing is realized by applying new gas enclosure characteristics for the EDC ice core (Fig. S4 - S6). See Table S1 for details. All remaining CDJ are shown in Fig. 3.

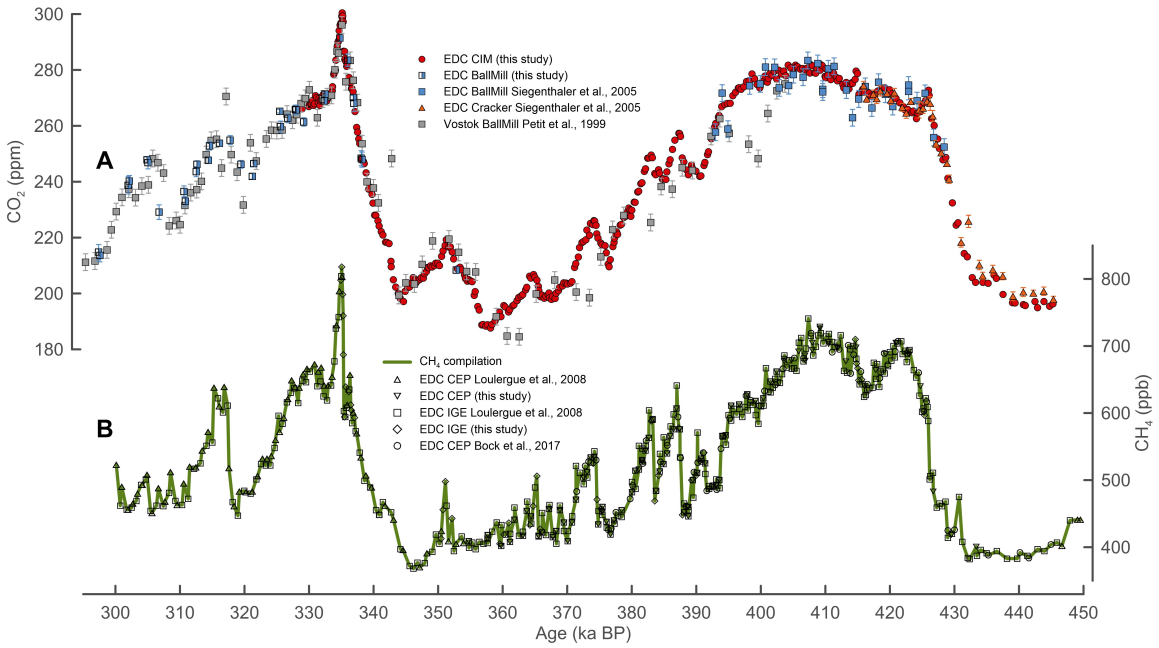

Fig. S2. Comparison between our CO_2 and CH_4 data from the EPICA Dome C (EDC) ice core with previously published data. (**A**) The new EDC CO_2 record overlaps with CO_2 data from the Vostok 5G ice core during 300 to 400 ka BP (*1*) and with previously published data from EDC during 390 to 450 ka BP (*2*). Note that the CO_2 data sets shown here were measured using three different dry extraction devices, namely the Centrifugal Ice Microtome (CIM) (*55*) and the Needle Cracker (*2*) employed at Climate and Environmental Physics (CEP), Physics Institute, University of Bern and the Ball Mill (*1, 2*) employed at the Institut des Géosciences de l'Environnement (IGE), Univ. Grenoble Alpes. (**B**) EDC CH_4 data, mainly based on data published by Ref. (*19*), complemented with new measurements (this study) and previously published data (*60*), all measured at CEP and IGE. Error bars for CH_4 are omitted for clarity. See legends for details.

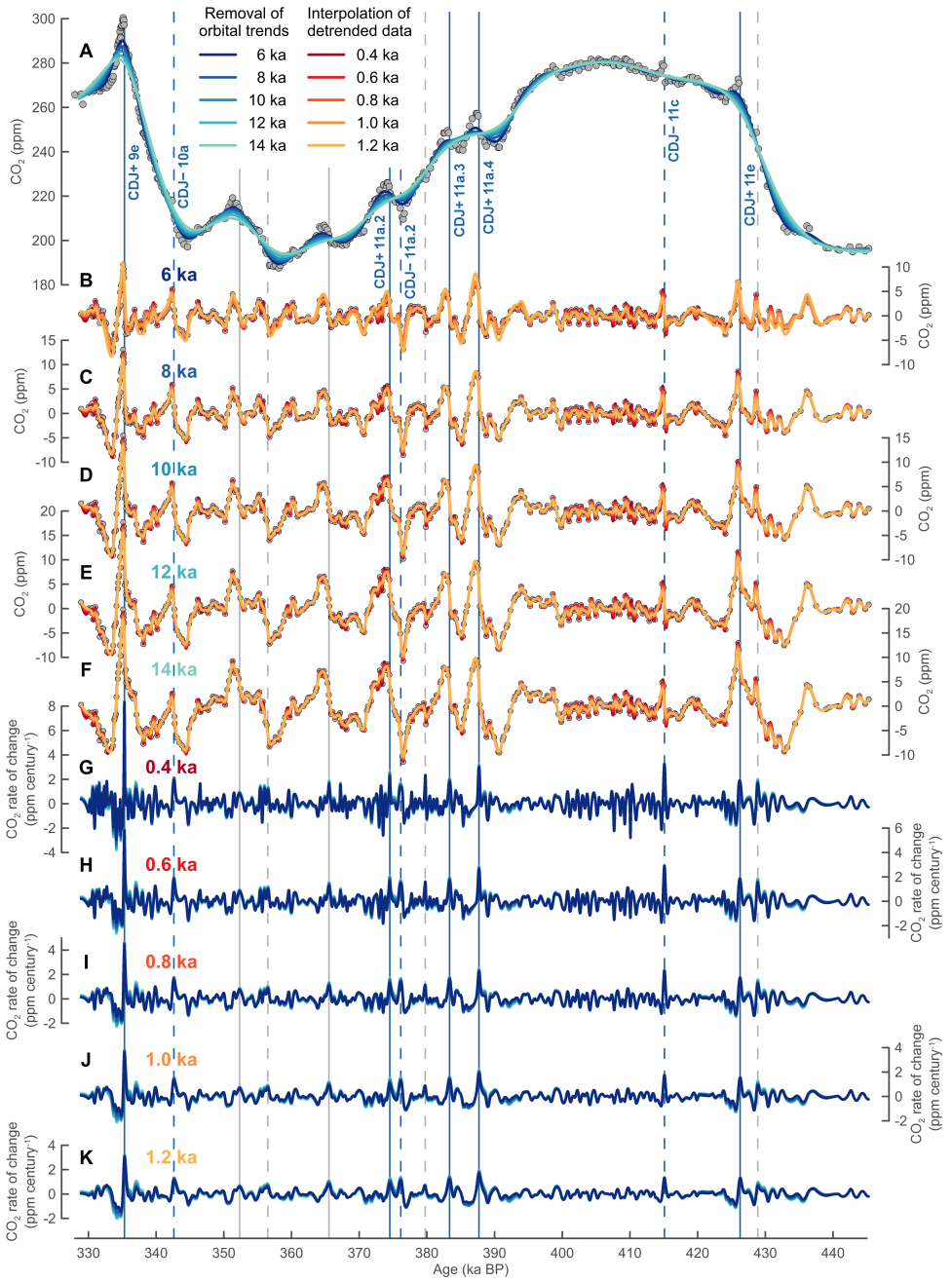

Fig. S3. Calculating the rate of change for our CO_2 record from the EPICA Dome C (EDC) ice core. (**A**) Removal of orbital to multi-millennial trends from the EDC CO_2 record (grey dots, this study) using five different smoothing splines (*75*) with cut-off periods (i.e., degrees of smoothing) ranging from 6 to 14 ka. (**B-F**) Detrended EDC CO_2 record after subtraction of splines shown in (A). A second set of five smoothing splines with cut-off periods ranging from 0.4 to 1.2 ka is applied onto the different detrended data sets, resulting in five times five annually resolved equidistant records containing only the centennial-scale variability. (**G-K**) Resulting rates of change of the detrended and interpolated CO_2 data from (B-F), grouped by their variant of spline interpolation. See legends for color-coding. Labelling and vertical lines are identical to Fig. 1.

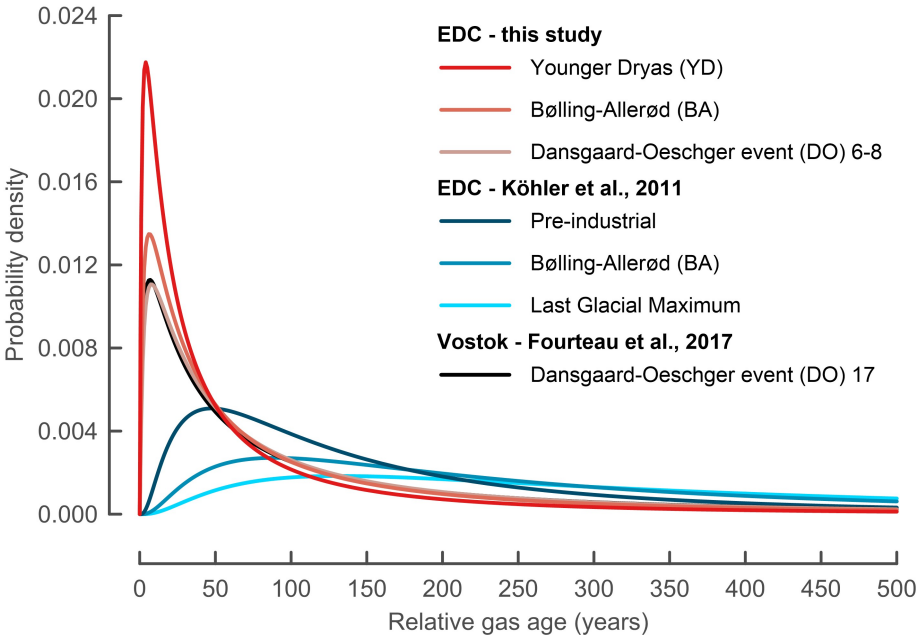

Fig. S4. Gas Age Distributions (GAD) for the low-accumulation sites EPICA Dome C (EDC) and Vostok for different climatic boundary conditions. All GAD shown here are represented by log-normal functions. The scenarios by Ref. (*79*) are approximations for the firn model outputs by Ref. (*77*), while our estimates are based on empirical smoothing of the West Antarctic Ice Sheet Divide (WD) CH_4 record to resemble the effective EDC CH_4 measurements (cf. Fig. S5, S6). The estimated GAD for the Preboreal (PB) is nearly congruent with the GAD for the Younger Dryas (YD) event and is omitted for clarity.

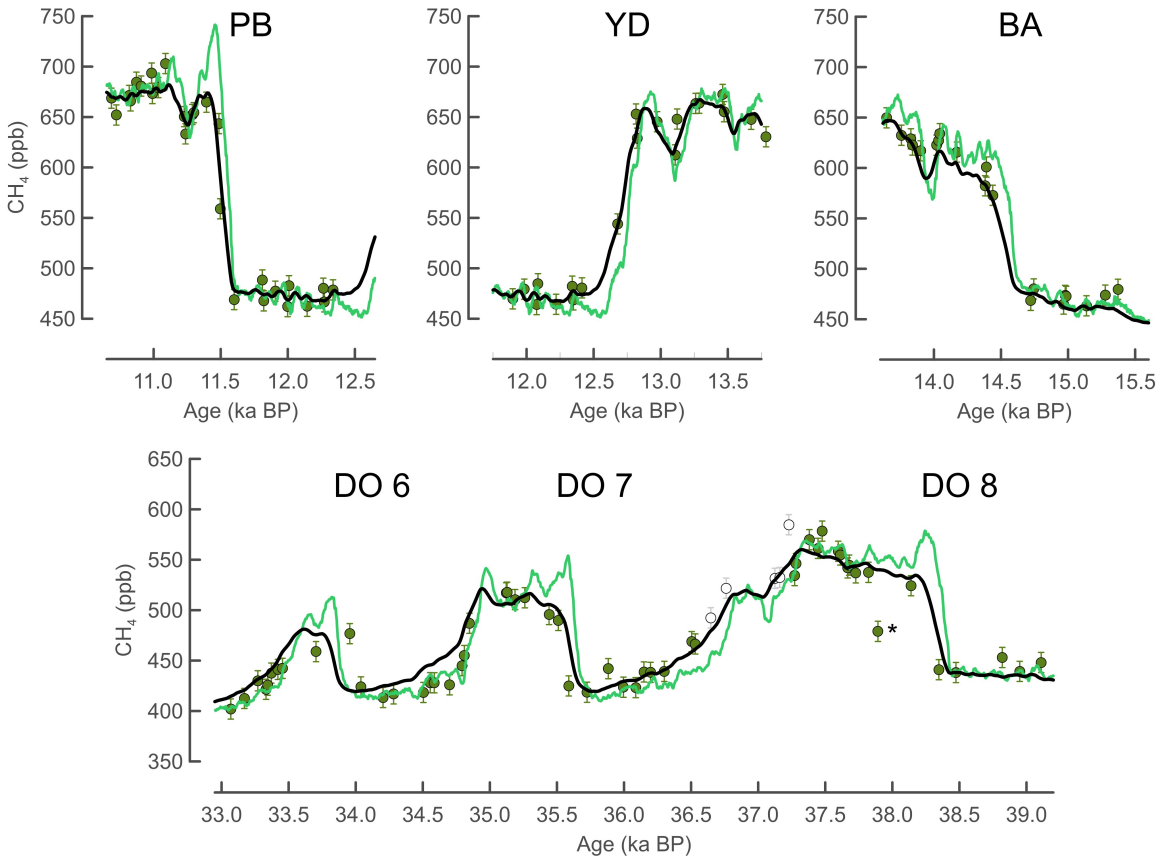

Fig. S5. Abrupt CH_4 transitions at the onsets of four different climatic periods during the last deglaciation and glacial period used for determining Gas Age Distributions (GAD) for the EPICA Dome C (EDC) ice core. These events include the onsets of the Preboral (PB), Younger Dryas (YD), and Bølling-Allerød (BA) during the last deglaciation (*21, 83*) and Dansgaard-Oeschger events (DO) 6 - 8 (*21, 34*) representative for firn column conditions during the colder glacial period. The black lines represent smoothed versions of the continuous West Antarctic Ice Sheet Divide (WD) ice core CH_4 data (light green lines) (*18*). The smoothed signals shown here (black lines) are produced using the mean values from 500 optimization iterations with the discrete EDC CH_4 data (green dots) varied within their uncertainty boundaries. White points in the lower panel lie outside the 2 ka optimization windows centered around the inflection points of the sharp CH_4 rises. The outlier (*) in the discrete EDC CH_4 data at 37.9 ka BP may be an artefact explained by staggered layering and has been excluded from the optimization runs (*80, 81*). See materials and methods for details.

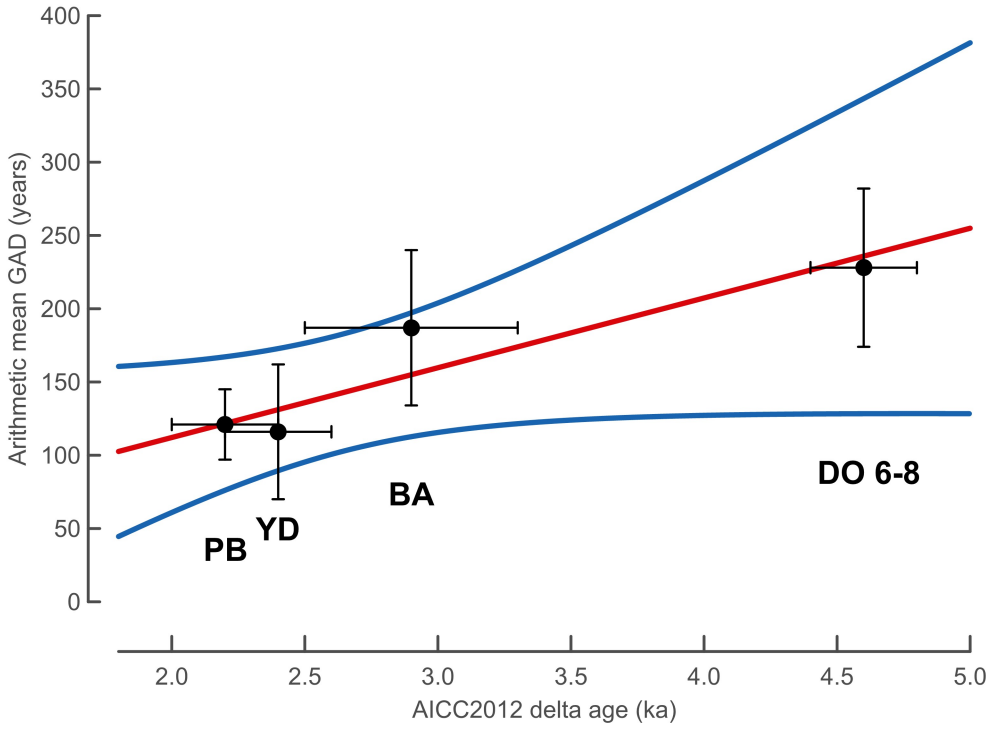

Fig. S6. Linear fit of optimized arithmetic mean values of estimated Gas Age Distributions (GAD) for the EPICA Dome C (EDC) ice core. The arithmetic means are based on a direct comparison between smoothed versions of the continuous CH_4 data from the West Antarctic Ice Sheet Divide (WD) ice core (*18*) and discrete data from EDC ice core (*21, 83*) (Fig. S5). The gas-ice difference (delta age) was determined using the AICC2012 age scale (*34*). Here we focus on the onsets of three key periods, including the Preboral (PB), Younger Dryas (YD), and Bølling-Allerød (BA) periods all characterized by abrupt CH_4 rises. In addition, we also include Dansgaard-Oeschger events (DO) 6 - 8 representative for firn column conditions during the colder glacial period. The used linear regression model (red line, R^2=0.85), including the 95% confidence intervals (blue lines), takes both variable uncertainties (±2 sigma) into account (*85*). All GAD are approximated by log-normal functions. See Fig. S5, Eq. S2, and materials and methods for details.

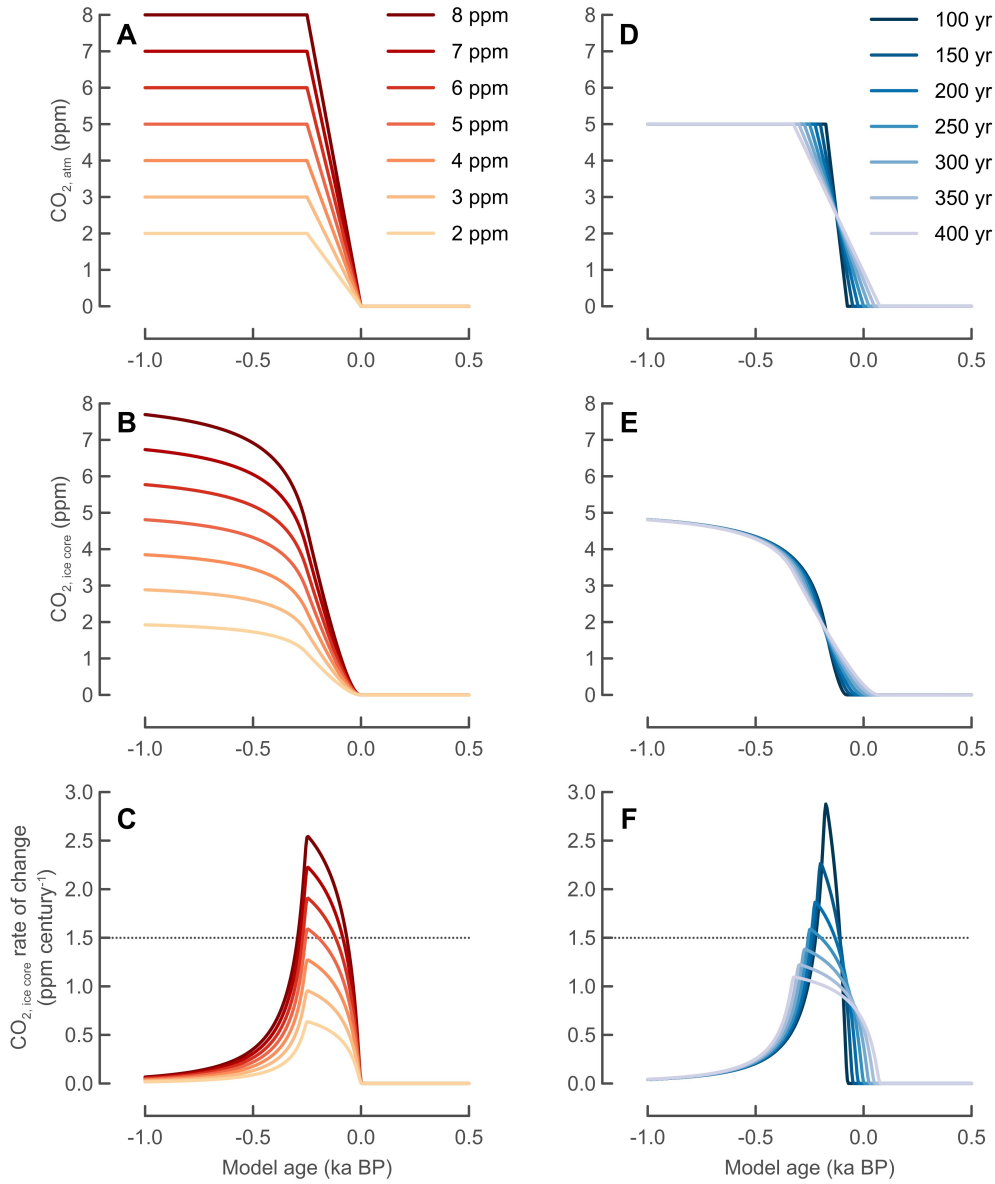

Fig. S7. Detection limit for Carbon Dioxide Jumps (CDJ). (**A**) Generic CDJ events (i.e., simple step functions) with atmospheric CO_2 rises ranging from 2 to 8 ppm and constant durations of 250 years. (**B**) Firn column smoothed version of (A) mimicking signals as they would be recorded by the EPICA Dome C ice core during the MIS 12a glacial maximum. MIS 12a represents the coldest interval associated with the strongest firn column-induced smoothing during MIS 9e - 12a. We estimate an arithmetic mean of 233±132 years for the Gas Age Distribution (GAD) at MIS 12a (Eq. S2) based on an estimated delta age of 4.5±0.3 ka (*34*) (see materials and methods for details). (**C**) Resulting rate of change of (B), comparable to what would be expected to be found in our ice core record (cf. Fig. S3). (**D-F**) Same as (A-C) but fixed 5 ppm CO_2 rises and changing durations (100 to 400 years). The dotted lines in (C) and (F) indicate the chosen threshold of 1.5 ppm per century in our CO_2 ice core record analyses (Fig. 1) used to identify CDJ events. See Fig. S8 for a comprehensive matrix of varying combinations of atmospheric CO_2 rises and durations. See supplementary text for details.

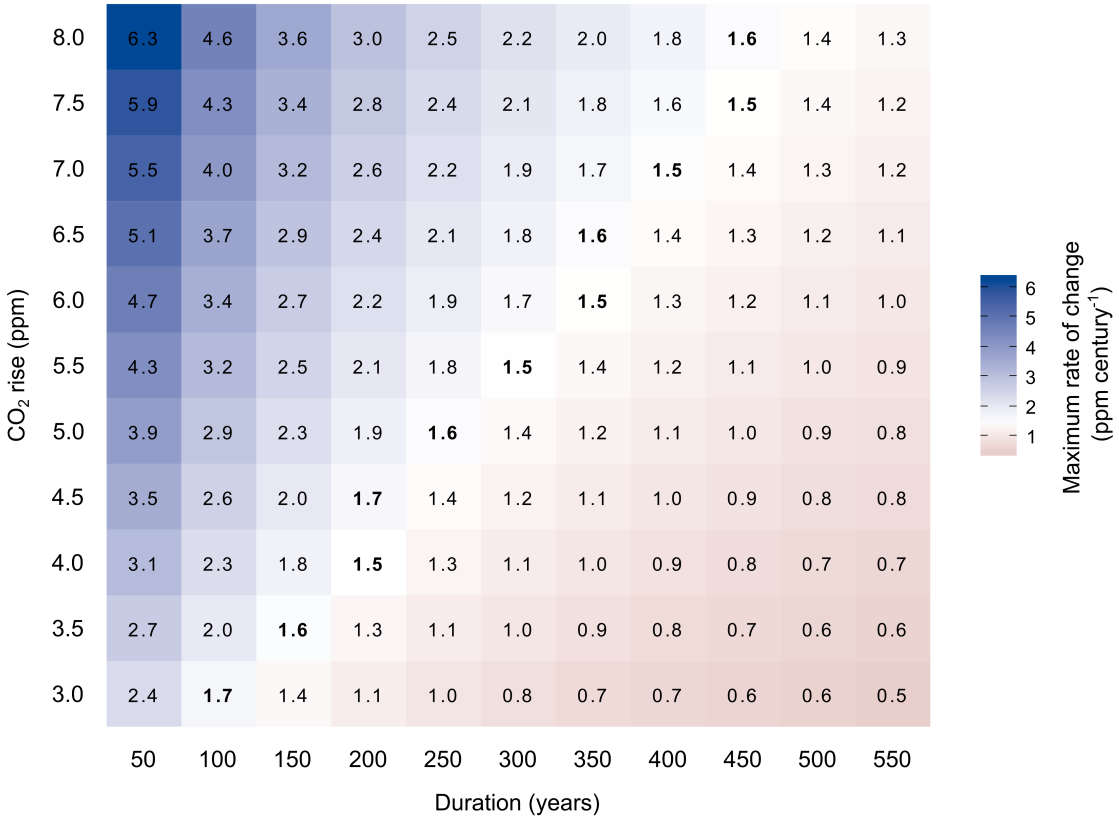

Fig. S8. Heat map of maximum amplitudes in the rates of change of generic Carbon Dioxide Jumps (CDJ) with varying atmospheric CO_2 rises and durations. Generic CDJ with CO_2 rises ranging from 3 to 8 ppm and durations ranging from 50 to 550 years in the atmosphere are smoothed to simulate a signal as it would be archived in the EPICA Dome C (EDC) ice core. Tiles represent peak values of the calculated rate of change of the simulated ice core signal. Identical methodologies to Fig. S7 are used (see supplementary text for details). All combinations of atmospheric CO_2 rises and durations exceeding the threshold value of 1.5 ppm per century in the ice core record would be identified as a CDJ in our EDC CO_2 record. For each magnitude of CO_2 rise (rows) the highest permissible duration that would just allow for CDJ detection is highlighted in bold.

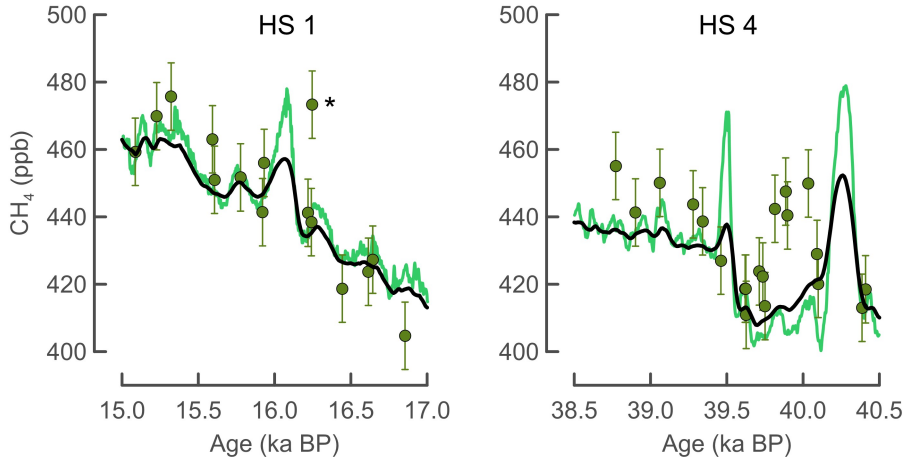

Fig. S9. Smoothing of short-lived overshoots in the CH_4 record in case of the EPICA Dome C (EDC) ice core. An estimation of the EDC firn column-induced smoothing (black line) of short-lived, small amplitude CH_4 overshoots (centered peaks) found in the continuous West Antarctic Ice Sheet Divide (WD) CH_4 record (light green line) for Heinrich Stadials (HS)1 and HS4 (*18*) during the last glacial period. The WD CH_4 record is smoothed using the linear relationship for EDC gas enclosure characteristics established in Fig. S6 (Eq. S2), assuming a gas-ice age difference (delta age) of 3.1±0.3 ka and 4.1±0.3 ka (*34*), resulting in GADs with arithmetic means of 166±103 years (HS1) and 214±123 years (HS4), respectively. Discrete EDC CH_4 data are shown as green dots. Note that mismatches in both records can be explained by age scale inconsistencies. The outlier in the EDC CH_4 record in close proximity to the HS1 WD CH_4 event (*) can likely be explained by staggered layering effects (*80, 81*) and should not be interpreted as an indicator for reduced smoothing of the EDC ice core.

Event	Duration (years)	CO_2 rise (ppm)	Growth rate (ppm century^{-1})	Delta age (ka)	GAD_{mean} (years)
CDJ+ 9e	59±35	15.8±1.1	26.2±17.6	1.8±0.3	103±82
CDJ− 10a	257±81	12.3±1.9	4.9±1.7	3.3±0.3	175±107
CDJ+ 11a.2	203±160	6.8±1.5	3.4±2.6	2.9±0.3	156±100
CDJ− 11a.2	540±170	10.0±1.8	1.9±0.5	3.0±0.3	161±102
CDJ+ 11a.3	225±176	6.7±1.3	3.0±2.1	2.9±0.3	156±100
CDJ+ 11a.4	140±110	9.3±1.2	6.9±6.7	2.9±0.3	156±100
CDJ− 11c	191±123	12.9±2.7	6.9±5.3	2.1±0.3	118±86
CDJ+ 11e	312±103	9.9±1.7	3.2±1.0	2.2±0.3	123±88

Table S1. Estimated atmospheric characteristics for identified Carbon Dioxide Jumps (CDJ). Estimates are based on empirically-derived gas enclosure (firn smoothing) characteristics for the EPICA Dome C (EDC) ice core, commonly referred to as Gas Age Distributions (GAD). The widths of the GAD (GAD_{mean}) are determined based on the ice-gas age difference (delta age) as derived from the AICC2012 age scale (*34*). See materials and methods, Fig. 3B, S1B, S6, and Eq. S2 for details. Note that in the case of CDJ+ 11e the duration is likely overestimated whereas the rate of change is likely underestimated. See supplementary text and Fig. S1 for details.

Data S1 (separate file). Antarctic ice core derived CO_2 and CH_4 data from the EPICA Dome C (EDC) ice core covering Marine Isotope Stage 9e - 12a. An additional compilation of the CH_4 data is provided in a separate worksheet. See materials and methods in the supplementary materials for details.

Data S2 (separate file). Marine sediment core derived planktic $\delta^{18}O$ *G. bulloides* and benthic $\delta^{18}O$ and $\delta^{13}C$ *C. wuellerstorfi* from the International Ocean Discovery Program (IODP) Site U1385 covering Marine Isotope Stage 9e - 12a. See materials and methods in the supplementary materials for details.